
Theses and Dissertations

Fall 2010

Observations of thermal creep gas flow and dust-density waves in dusty plasma experiments

Timothy McGuire Flanagan
University of Iowa

Copyright 2010 Timothy McGuire Flanagan

This dissertation is available at Iowa Research Online: <http://ir.uiowa.edu/etd/802>

Recommended Citation

Flanagan, Timothy McGuire. "Observations of thermal creep gas flow and dust-density waves in dusty plasma experiments." PhD (Doctor of Philosophy) thesis, University of Iowa, 2010.
<http://ir.uiowa.edu/etd/802>.

Follow this and additional works at: <http://ir.uiowa.edu/etd>

 Part of the [Physics Commons](#)

OBSERVATIONS OF THERMAL CREEP GAS FLOW AND DUST-DENSITY
WAVES IN DUSTY PLASMA EXPERIMENTS

by

Timothy McGuire Flanagan

An Abstract

Of a thesis submitted in partial fulfillment of the
requirements for the Doctor of Philosophy
degree in Physics in the
Graduate College of The
University of Iowa

December 2010

Thesis Supervisor: Professor John A. Goree

ABSTRACT

In laboratory experiments, I study strongly-coupled dusty plasma levitated in a glow-discharge plasma. Dusty plasma is an arrangement of small dust particles in a plasma background of electrons, ions, and neutral gas. The dust particles are negatively charged because they collect electrons and ions from the background plasma. Depending on the experimental setup, the plasma's electric field can help to balance the dust particles against gravity. The high dust charge causes dust particles to repel each other, while confinement forces prevent their escape. The dust particles cannot easily move past one another, and instead organize themselves into highly-ordered structures. The neutral gas also plays a key role in these experiments. Depending on the relative motion between gas and dust particles, the neutral gas can either impede dust motion or it can drive the dust into motion.

In this thesis, I report the findings of three separate experiments. In the first experiment, I use a spherically-shaped dusty plasma (Yukawa ball) as an indicator of a flow of neutral gas, called thermal creep flow. In the second and third experiments, I study naturally occurring dust-density waves, which propagate within the volume of a dusty plasma that has many horizontal layers.

In Ch. 2 of this thesis, I study thermal creep flow (TCF), which is a flow of gas driven by a temperature gradient along a solid boundary. Stripes on a glass box are heated by laser beam absorption, leading to both TCF and a thermophoretic force. A stirring motion of the dust particle suspension is observed. By eliminating all other explanations for this motion, I conclude that TCF at the boundary couples by drag to the bulk gas, causing the bulk gas to flow, thereby stirring the suspension of dust particles. This result provides an experimental verification that TCF in the slip-flow regime causes steady-state gas flow in a confined volume.

In Ch. 3, I observe the growth of a naturally occurring dust-density wave (DDW) using high-speed imaging. This low-frequency wave (~ 25 Hz) grows in amplitude as it propagates downward through a dusty plasma. I measure the wave's linear growth rate using a phase-sensitive analysis method. For the conditions studied here, the growth rate increases as gas pressure decreases. At a critical gas pressure that I observe, a balance between an ion-flow instability and dissipation by neutral gas drag determines a threshold for wave propagation. A linear dispersion relation is derived, taking into account effects of strong coupling, to compare to the experiment.

In Ch. 4, I observe the development of nonlinearity in the naturally occurring dust-density wave by measuring harmonics of the fundamental. Using high-speed imaging, I measure amplitudes, wave numbers and growth rates for the fundamental and its harmonics. The amplitudes of the harmonics exhibit a strong exponential increase with diminishing gas pressure, and they saturate at lower gas pressures. My measurements show that the wave numbers and growth rates of harmonics are near integer multiples of the fundamental.

Abstract Approved: _____
Thesis Supervisor

Title and Department

Date

OBSERVATIONS OF THERMAL CREEP GAS FLOW AND DUST-DENSITY
WAVES IN DUSTY PLASMA EXPERIMENTS

by

Timothy McGuire Flanagan

A thesis submitted in partial fulfillment of the
requirements for the Doctor of Philosophy
degree in Physics in the
Graduate College of The
University of Iowa

December 2010

Thesis Supervisor: Professor John A. Goree

Copyright by
TIMOTHY MCGUIRE FLANAGAN
2010
All Rights Reserved

Graduate College
The University of Iowa
Iowa City, Iowa

CERTIFICATE OF APPROVAL

PH.D. THESIS

This is to certify that the Ph.D. thesis of

Timothy McGuire Flanagan

has been approved by the Examining Committee
for the thesis requirement for the Doctor of
Philosophy degree in Physics at the December 2010
graduation.

Thesis Committee: _____
John A. Goree, Thesis Supervisor

Frederick N. Skiff

Robert L. Merlino

Gregory Howes

Albert Ratner

To Erin and Bill

ACKNOWLEDGMENTS

I would like to thank my advisor John Goree for his invaluable guidance and teaching over my graduate education. I will reap benefits from his mentoring that will last throughout my professional career.

The work in Chapter 2 was supported by NASA and DOE. I would like to thank J. Goree who is co-author of our publication of these findings, and O. Arp for instruction and helpful discussions regarding confinement of Yukawa balls.

The work in Chapters 3 and 4 was supported by NASA and NSF. I would again like to thank J. Goree, who will be co-author of the publications of this work. I would also like to thank F. Skiff and R.L. Merlino for helpful discussions.

ABSTRACT

In laboratory experiments, I study strongly-coupled dusty plasma levitated in a glow-discharge plasma. Dusty plasma is an arrangement of small dust particles in a plasma background of electrons, ions, and neutral gas. The dust particles are negatively charged because they collect electrons and ions from the background plasma. Depending on the experimental setup, the plasma's electric field can help to balance the dust particles against gravity. The high dust charge causes dust particles to repel each other, while confinement forces prevent their escape. The dust particles cannot easily move past one another, and instead organize themselves into highly-ordered structures. The neutral gas also plays a key role in these experiments. Depending on the relative motion between gas and dust particles, the neutral gas can either impede dust motion or it can drive the dust into motion.

In this thesis, I report the findings of three separate experiments. In the first experiment, I use a spherically-shaped dusty plasma (Yukawa ball) as an indicator of a flow of neutral gas, called thermal creep flow. In the second and third experiments, I study naturally occurring dust-density waves, which propagate within the volume of a dusty plasma that has many horizontal layers.

In Ch. 2 of this thesis, I study thermal creep flow (TCF), which is a flow of gas driven by a temperature gradient along a solid boundary. Stripes on a glass box are heated by laser beam absorption, leading to both TCF and a thermophoretic force. A stirring motion of the dust particle suspension is observed. By eliminating all other explanations for this motion, I conclude that TCF at the boundary couples by drag to the bulk gas, causing the bulk gas to flow, thereby stirring the suspension of dust particles. This result provides an experimental verification that TCF in the slip-flow regime causes steady-state gas flow in a confined volume.

In Ch. 3, I observe the growth of a naturally occurring dust-density wave (DDW) using high-speed imaging. This low-frequency wave (~ 25 Hz) grows in amplitude as it propagates downward through a dusty plasma. I measure the wave's linear growth rate using a phase-sensitive analysis method. For the conditions studied here, the growth rate increases as gas pressure decreases. At a critical gas pressure that I observe, a balance between an ion-flow instability and dissipation by neutral gas drag determines a threshold for wave propagation. A linear dispersion relation is derived, taking into account effects of strong coupling, to compare to the experiment.

In Ch. 4, I observe the development of nonlinearity in the naturally occurring dust-density wave by measuring harmonics of the fundamental. Using high-speed imaging, I measure amplitudes, wave numbers and growth rates for the fundamental and its harmonics. The amplitudes of the harmonics exhibit a strong exponential increase with diminishing gas pressure, and they saturate at lower gas pressures. My measurements show that the wave numbers and growth rates of harmonics are near integer multiples of the fundamental.

TABLE OF CONTENTS

LIST OF TABLES	viii
LIST OF FIGURES	ix
CHAPTER	
1 INTRODUCTION	1
2 GAS FLOW DRIVEN BY THERMAL CREEP IN DUSTY PLASMA	6
2.1 Introduction	6
2.2 Gas Flow and Temperature Gradients	8
2.3 Experimental Design	10
2.3.1 Apparatus	11
2.3.2 Localized heating	12
2.3.3 Detecting gas flow with dusty plasma	14
2.3.4 Temperature measurements	15
2.4 Results	16
2.4.1 Plasma effects vs temperature gradients	17
2.4.2 Thermophoretic force vs gas drag force	19
2.4.3 Thermal creep flow vs. free convection	20
2.5 Summary	22
3 OBSERVATION OF THE SPATIAL GROWTH OF SELF-EXCITED DUST-DENSITY WAVES	24
3.1 Introduction	24
3.2 Experimental Design	27
3.3 Observations	30
3.4 Analysis	31
3.4.1 Space-time diagrams	33
3.4.2 Dominant frequency	34
3.4.3 Amplitude and phase	35
3.5 Growth Rate Results	36
3.6 Fluid Model for Linear Waves	39
3.7 Experiment vs Linear Wave Theory	45
3.8 Summary	46
4 DEVELOPMENT OF NONLINEARITY IN A GROWING SELF- EXCITED DUST-DENSITY WAVE	47
4.1 Introduction	47
4.2 Experimental Design	49
4.3 Wave Amplitude Observations	52

4.4	Analysis Methods	52
4.5	Results	54
4.5.1	Fundamental frequency	54
4.5.2	Nonlinear development with diminishing pressure	54
4.5.3	Wave numbers and growth rates of harmonics	58
4.6	Summary	62
5	SUMMARY	64
APPENDIX		
A	ESTIMATES OF DDW EXPERIMENTAL PARAMETERS	67
REFERENCES		69

LIST OF TABLES

A.1	Experimental Input Parameters for Linear Wave Model	68
-----	---	----

LIST OF FIGURES

2.1	Laser heating a glass surface and driving a gas flow. A green vertical laser sheet is used to heat two stripes on a glass box, as illustrated from the (a) perspective view (dust not shown) and (b) top view (dust shown). The laser sheet strikes two faces of the box, creating two heated stripes (shown in red and indicated with two arrows), but does not strike dust. The laser sheet is shown both in the interior (light green) and exterior (dark green) of the box. (c) Sketch of gas flow arising from tangential temperature gradients at a glass-gas boundary. In the rarefied gas near the boundary, TCF occurs; this couples to the bulk gas farther from the boundary, causing it to flow also. Flow of the bulk gas disturbs the dust suspension, which is imaged. (d) Glass temperature, measured under the same vacuum conditions but without plasma, <i>vs.</i> horizontal distance from each of two heated stripes.	13
2.2	Top view of dust particle positions, from separate tests using (a) the heated box that absorbs light and (b) the control box that does not absorb light. Each panel shows dust particle positions in a horizontal plane before laser application (blue circles) and during laser application (red triangles). The origin is the horizontal center of the glass box. A laser sheet strikes the two faces of the box, as in Fig. 2.1(a) and 2.1(b). In the test with the heated box, the dust suspension (Yukawa ball) is <i>displaced</i> away from the heating laser beam to a new <i>horizontal</i> equilibrium position. This displacement is attributed to the thermophoretic force.	18
2.3	Top view of the steady-state dust velocity field \vec{V} (black arrows) and vorticity $\vec{\nabla} \times \vec{V}$ (color map) in units of s^{-1} . Gravity is into the page. The origin is the equilibrium center of the Yukawa ball. Data shown are dust velocities mapped to a regular grid (40×30), and averaged over the movie's last 100 frames (2 s). The stirring of dust into a horizontal flow is the main result that I seek to explain.	19
2.4	Side view of the steady-state dust velocity field \vec{V} (black arrows) and vorticity $\vec{\nabla} \times \vec{V}$ (color map) in units of s^{-1} . Gravity is directed downward. The origin is the equilibrium center of the Yukawa ball. Data shown are averaged and scaled as in Fig. 2.3. Comparing to Fig. 2.3 shows that the flow of dust is predominantly horizontal, indicating that the flow of bulk gas is also predominantly horizontal.	20

2.5	Time series of kinetic energy of dust particles in a horizontal plane averaged over five runs (black circles) and of particles in a vertical plane averaged over two runs (red squares). The laser heating is applied at $t = 5$ s. Dust motion in the vertical direction is much weaker than in the horizontal. The comparison of vertical <i>vs.</i> horizontal motion here and in Fig. 2.4 leads me to eliminate free convection as the cause of the observed stirring in Fig. 2.3. Each datum is averaged over all non-zero gridpoints in the 40×30 field of view and then over 100 contiguous frames (2 seconds).	21
3.1	Sketch of the experimental setup. In a radio-frequency argon plasma, dust particles are levitated within the volume of a glass box, forming a dusty plasma. A laser sheet illuminates dust in a vertical plane and the dust cloud is imaged from the side with a digital video camera. For each movie, images are recorded at 500 frames per second for 2.048 seconds.	28
3.2	Single side view images of the dust cloud's central region. Bright spots are individual dust particles. Depending on the gas pressure, energy from a downward ion flow can couple to dust motion, causing nearly planar compressional waves to be excited and propagate in the $-\hat{z}$ direction. (a) At the starting pressure of 426 mTorr, no wave is observed. Under these stable conditions, dust particles are mainly arranged in horizontal layers. (b) Near a critical pressure of 424 mTorr the effect of ion flow barely overcomes gas damping, and a small amplitude wave grows as it propagates downward. The wave fronts are visible in the still image. (c) and (d) At lower pressures, ion flow more effectively couples to dust motion, and the wave grows at a faster rate, reaching larger amplitudes. Each panel shows the same $3.57 \text{ mm} \times 5.29 \text{ mm}$ spatial region. Gravity is downward.	29
3.3	Image showing the DDW propagating downward through the dust cloud at the critical gas pressure of 424 mTorr. The white rectangle indicates the spatial region that is analyzed. It is the same region that is shown in each panel in Fig. 3.2. Within this region, the wave fronts are sufficiently planar to justify a one-dimensional analysis.	31
3.4	Portions of space-time diagrams for pressures (a) 424 mTorr and (b) 410 mTorr. Gray scale maps like these are the basis for all my analysis. The bright equally-spaced sloped lines indicate wavefronts. Amplitudes grow as the wave propagates downward.	32
3.5	The dominant frequency f exhibits a slight downward trend with gas pressure. The data points shown are the result of calculating the power spectrum of the space-time diagram.	34

3.6	Spatial profiles of the dust-density wave's (a) phase $\phi(z)$ and (b) amplitude $A(z)$ for three gas pressures. These profiles are computed using the method described in Sec. 3.4.3. The growth is more rapid at lower gas pressures. Amplitude data (plotted log-linear) reveal exponential growth as the wave propagates downward. The growth rates are quantified by fitting the profiles to an exponential (straight dashed lines).	38
3.7	Variation with gas pressure p of (a) spatial growth rate k_i and (b) frequency f . The errors in the experimental k_i measurements shown here reflect variations due to the arbitrary choice of the range of z used in fitting the amplitude profile. Solid curves for the theory assume experimental parameters listed in Table A.1 (Appendix). . .	39
3.8	Theoretical dispersion relation (solid curves) for a gas pressure of 410 mTorr, calculated from Eq. 3.6. The real frequency is plotted in blue and the spatial growth rate in magenta. The most unstable k -mode predicted by the theory is close to the experimentally measured frequency and growth rate, which are shown as crosses. The model's input parameters are listed in Table A.1.	44
4.1	Time series measurement of gas pressure p , which is the experimental parameter used to control the instability and growth of the dust-density wave. The pressure is constant until time $t = 0$, when p begins to decrease at a linear rate. At the same time, a movie begins recording, which provides the principal data for the experiment. . .	50
4.2	Side-view images of the dust cloud's central region. Bright spots are individual dust particles. Depending on the gas pressure, the ion-flow instability can cause planar compressional waves to grow in amplitude as they propagate downward in the $-\hat{z}$ direction. (a) At the highest pressure, gas damping causes the wave to be barely detectable. (b)-(d) At lower gas pressures, gas damping is less effective and the wave grows to higher amplitudes, as indicated by the bright high-density wave fronts near the bottom of the dust cloud. Each panel shows the same $2.95 \text{ mm} \times 5.90 \text{ mm}$ spatial region.	51
4.3	Power spectra plotted vs. vertical position z for three gas pressures. The fundamental frequency is $f = 25.0 \text{ Hz}$. (a) At high gas pressures, I can detect only the fundamental and only at lower values of z . (b)-(c) At lower pressures, harmonics become stronger. At 417 mTorr, I can detect all nine harmonics that are below the Nyquist frequency of 250 Hz (half the camera's frame rate); only the first four harmonics are shown. These spectra are calculated from the space-time data. Each panel corresponds to a sequence of 1024 frames, i.e. 2 s of data, centered at the times indicated.	55

- 4.4 Development of nonlinearity. (a) Amplitudes of the fundamental A_1 , the second harmonic A_2 and the third harmonic A_3 . As pressure p decreases, the amplitudes increase exponentially from noise levels and then saturate. The amplitudes are calculated for a position near the bottom of the dust cloud. (b) Total harmonic distortion (THD), an indicator of nonlinearity, calculated from the amplitudes in (a). After emerging from noise, the THD increases exponentially as p decreases, with a pressure constant p_o , and then saturates. At saturation, THD= 45%, i.e, the harmonic energy is almost half the fundamental energy. Noise at higher pressures is due to small wave amplitudes. In both panels, the gas pressure scale is reversed (bottom axis). Results here and in Fig. 4.6 are computed from the space-time data using phase-sensitive detection. 57
- 4.5 Vertical profiles of (a)-(c) the wave's phase ϕ and (d) the wave's amplitude A , corresponding to gas pressure $p = 416.8$ mTorr. Results are shown for the fundamental wave mode (ϕ_1, A_1) and its second and third harmonics, (ϕ_2, A_2) and (ϕ_3, A_3) . Profiles like these are calculated from space-time data using phase-sensitive detection. These profiles are then used to measure the wave numbers k_r and growth rates $-k_i$ 59
- 4.6 Measurements of (a) wave numbers k_r and (b) growth rates $-k_i$ as a function of gas pressure p . In panel (a), the real wave numbers for the fundamental mode k_{r1} , second harmonic k_{r2} , and third harmonic k_{r3} do not vary with p . In panel (b), the growth rates of the same modes $-k_{i1}$, $-k_{i2}$, $-k_{i3}$ increase slightly as p decreases. (c) Wave number ratios k_{r2}/k_{r1} and k_{r3}/k_{r1} are close to two and three, respectively, when nonlinearity develops at lower pressures. (d) Growth rate ratios k_{i2}/k_{i1} and k_{i3}/k_{i1} are also two and three. In panels (a) and (b), scatter at higher pressures is due to small wave amplitudes, which lead to noise in measurements of k_r and k_i . In panels (c) and (d), adjacent averaging is used to smooth data before calculating the ratios. Pressure and time scales are the same as in Fig. 4.4. 60

CHAPTER 1 INTRODUCTION

A plasma can be loosely defined as an ionized gas, consisting of electrons, ions, and often neutral gas. Although the air around us is almost entirely neutral gas, the vast majority of the universe is made up of plasma. Common examples are the Sun (or any star), the interstellar medium, and the Earth's ionosphere. While plasma is not often found naturally in our daily lives, there are exceptions. A few examples of everyday plasma are lightning, the interior of light bulbs, a welding arc, and perhaps an extremely hot flame. Despite the few examples of plasma on Earth, they are easily and readily produced in the laboratory.

A dusty plasma, often termed complex plasma, is a suspension of small dust particles in a background of electrons, ions, and neutral gas. Dusty plasma was originally of interest to those who studied astrophysics [1]. Well-known astronomical dusty plasmas include planetary ring systems and the tails of comets [2, 3]. Dusty plasma is also of special importance in industrial applications such as semiconductor manufacturing [4, 5], where macroscopic dust particles often form out of the gas phase in reactive plasmas. When the plasma is shut off, the dust particles then fall onto the substrate, contaminating the wafer. Thus, in many plasma processing applications, dust is a nuisance that should be avoided if possible, or at least mitigated. However, it has been suggested that dust could be useful in certain photovoltaics applications [6], where the presence of dust would actually increase deposition rates.

One of the biggest advantages of studying dusty plasma in the laboratory is that dust particles can often be tracked individually. Compared to electrons and ions, the dust particles have a very large mass. The mass of dust particles is often so large that the time scales of their dynamics are sufficiently long enough

to be observed visually. This allows for, if desired, a kinetic analysis in which the position and velocity of individual particles are measured. This tracking is done by illuminating the dust particles with a laser, and then imaging them with a camera. Many simple techniques have been developed to accurately calculate the positions of particles in the images [7]. If the image analysis does not require particle tracking, then physical information can be inferred directly from the raw images recorded by the camera.

When a small dust particle (usually a few microns or smaller) is immersed in a plasma, the dust becomes charged by absorbing electrons and ions from the background plasma. Because electrons are much less massive than ions, electrons have a higher thermal velocity. For this reason, dust particles in a laboratory plasma tend to charge negatively, which is crucial for their levitation. For an isolated spherical dust particle immersed in a plasma, the negative charge acquired Q_d depends on the radius of the dust particle r_d and its floating potential relative to the plasma V_f according to $Q_d = (4\pi\epsilon_0 r_d)V_f$, where ϵ_0 is the permittivity of free space. The dust particle's floating potential is the potential at which the electron and ion currents balance, and largely depends on the electron temperature T_e . As an example, for a dust particle immersed in a hydrogen plasma [2], $V_f = -2.51(k_B T_e/e)$, where k_B is Boltzmann's constant and e is the electron charge. Thus, an isolated 1- μm dust particle immersed in a hydrogen plasma with an electron temperature of 3 eV has a charge of about $-5000e$. While very simple and intuitive, this isolated dust charging model does not take into account other effects that can be important in dusty plasma, such as the depletion of plasma by the dust particles. When the dust number density is large, plasma depletion can cause a significant reduction in the dust floating potential, which in turn reduces the dust charge [8].

Because they are charged, dust particles can be confined indefinitely in a

plasma. This confinement is accomplished by forces acting on the dust particle in the plasma. In the vertical plane, the downward forces of gravity (and sometimes the smaller ion drag force) are balanced by an upward electric force due to a natural electric field in the plasma. This upward electric force can be augmented by a thermophoretic force [9], as is done in Ch. 2 of this thesis. In the horizontal plane, the mutually repulsive forces between negatively-charged dust particles are balanced by the plasma's horizontal electric fields.

In ground-based experiments, the dust particles settle into regions of strong vertical electric fields, where the electric force is strong enough to balance gravity. These strong field regions are in the so-called plasma sheath, which is near solid surfaces such as the electrode. In the sheath, there is an imbalance of the electron and ion density, resulting in a large electric field. It is often the case that dust particles are the same size, and thus acquire the same charge. For this reason, they settle at the same vertical height forming planar lattices. However, if the horizontal electric fields are comparable in strength to the vertical fields, the suspension of particles can fill a volume, as is the case in experiments reported in this thesis.

In these experiments, I use a glass box to provide strong horizontal confining forces. The glass box has vertically-oriented walls, and is placed atop a horizontally-oriented electrode. The presence of the box walls alters the electric potential profile in the plasma [10]. The result is a sheath both in the horizontal direction and the vertical direction, allowing for the confinement of a dusty plasma that fills a volume, instead of a two-dimensional plane.

In addition to confining forces, dust particles also experience a force due to gas drag. As stated above, the laboratory plasma contains neutral gas. Collisions between dust particles and gas atoms can either dissipate dust motion or drive it, depending on the relative motion between gas and dust. There will be examples of

both in this work. In Ch. 2, a flow of gas accelerates dust into motion, providing visual evidence of the gas flow. In Ch. 3 and Ch. 4, the presence of neutral gas contributes to the damping of a dust-density wave, in competition with the instability that drives the wave.

I perform three separate experiments in this thesis. In the first experiment, I use a spherically-shaped dusty plasma, called a Yukawa ball, to serve as an indicator of a gas flow called thermal creep flow (TCF). In this experiment, the neutral gas is just as important as the plasma, if not more so. Dust particles in the dusty plasma merely serve as an indicator of gas flow. The plasma forces just provide the necessary confinement for dust levitation. In the experiment, a laser is used to locally heat the surface of a glass box, causing a temperature gradient that drives thermal creep flow. This gas flow then couples to the dust particles via the gas drag force, accelerating them into motion. The design of the experiment allows for eliminating all possible explanations for the dust motion, except for the presence of thermal creep flow.

The second and third experiments both involve naturally occurring dust-density waves, or dust-acoustic waves. These waves propagate downward through a dusty plasma with many horizontal layers. The plasma's natural flow of ions is the free energy source for an instability. This ion-flow instability excites a compressional wave in the dusty plasma, similar to the well-known ion-acoustic wave in plasma physics, or even just a regular sound wave. The wave motion in the dust is damped by gas drag, and can entirely suppress the wave if the gas pressure is sufficiently high. Whether or not the wave exists is decided by a competition between the ion-flow instability and the damping due to gas drag. While the strength of the ion flow is largely decided by the plasma, the gas pressure is easily controlled by the experimenter.

In the second experiment, I measure the wave's linear growth rate just near the instability threshold for a series of gas pressures. I also compare the results with a fluid model that is adapted to account for strong coupling amongst the dust particles. In the third experiment, I observe the development of nonlinearity in the dust-density wave. The nonlinearities are identified by detecting harmonics in the wave as I ramp down the gas pressure. By measuring both the wave numbers and growth rates of the fundamental mode and its harmonics, I find that they are related in a very simple way.

CHAPTER 2

GAS FLOW DRIVEN BY THERMAL CREEP IN DUSTY PLASMA

2.1 Introduction

Thermal creep flow (TCF) is a flow of gas driven by a gas temperature gradient along a solid boundary. Since gas flows along the boundary, TCF is very different from the usual no-slip boundary conditions used in the Navier-Stokes model of gas (fluid) flow. The width of this boundary flow is on the order of a gas mean free path λ .

Although TCF occurs near a solid boundary, it does influence gas flow in other regions. As a result of collisions between neutral gas atoms, the *boundary* gas flow TCF can still drive a slower flow of the *bulk* gas. Here, bulk gas refers to gas in a region that is many mean free paths from the solid boundary. Faster atoms near the boundary can transfer momentum to atoms in the bulk gas via collisions, resulting in a directed flow of the bulk gas.

The effect of TCF was discovered by Reynolds [11] and then theoretically quantified by Maxwell in the last year of his life [12]. Today, industrial applications that exploit TCF include chemical vapor deposition in integrated circuit fabrication [13] and crystal growth [14]. Despite the importance of these applications, experiments to detect TCF are rare [15, 16, 17]. The literature for TCF mostly consists of reports of numerical simulations [18, 19, 20, 21, 22, 23, 24, 25].

Observing TCF experimentally poses a number of challenges. This kind of flow occurs within a few mean free paths of a heated surface. At atmospheric pressure it would be limited to micron-size regions, which are too small for most flow detection schemes. This size limitation can be relaxed by making measurements under vacuum conditions, where mean free paths are larger, but fewer sensors are practical. When it is impractical to position a sensor within a few mean free paths

of a surface, one must measure the flow of bulk gas that is driven by TCF, yielding an indirect detection of TCF.

The earliest experiment designed to detect TCF was performed using a windmill as a sensor and a bell jar to provide vacuum conditions [15, 16]. The heated surface was a glass plate. The mean free path was < 1 mm, much smaller than the windmill. The windmill was located 11 mm from the glass plate. Although the authors in Ref. [15, 16] did not discuss TCF and flow of bulk gas separately, we can interpret their experiment as detecting flow in the bulk gas because the sensor was located many mean free paths from the surface. Thus, their results rely on recognizing that a flow of bulk gas can be driven by TCF. Moreover, other causes of bulk gas flow, such as free convection, must be eliminated. The windmill experiment was designed so that the effects of free convection could be contrasted with those of TCF.

Dusty plasma is a suspension of small micron-size dust particles in a background of electrons, ions, and neutral gas. The dust becomes charged by absorbing electrons and ions. Dusty plasma is of special importance in industrial applications such as semiconductor manufacturing [4, 5] as well as in astrophysics [1].

The dusty plasma literature has long recognized the importance of the thermophoretic force in both experiment [9, 26] and theory [27], but it has only recently recognized TCF [17]. As the main result of this chapter, I report an experiment verifying the recent discovery [17] that TCF can have a large effect on dusty plasma. The result also serves as a rare experimental demonstration of TCF, for the fluid mechanics community. In both experiments (here and in Ref. [17]) nonuniform temperature gradients are purposely set up to drive TCF, evidenced by the effect this gas flow has on the dusty plasma.

Dust particles can be confined indefinitely in a plasma. This confinement is

accomplished by forces acting on the dust particles in the plasma. In the vertical direction, the downward force of gravity is balanced by an upward electric force due to a natural electric field in the plasma, which is sometimes augmented by an upward thermophoretic force [9]. In the horizontal direction, the mutually repulsive forces between negatively-charged particles are balanced by natural horizontal electric forces.

Additional forces, for example due to gas flow, can set dust particles into motion while confinement forces prevent their escape. In this experiment, the result of additional forces can have two observable effects: the entire suspension can be *displaced* to a new equilibrium position, and the dust suspension can be *stirred* so that dust particles circulate within the suspension. In this thesis, it will be argued that an overall displacement indicates a conservative force, whereas an observation of stirring indicates the presence of a gas flow.

The visible motion of dust particles suspended in a dusty plasma serves as an indicator of TCF. Because of their small mass and lack of frictional contact with solid surfaces, dust particles move easily in response to ambient gas flow and small forces. The dust suspension will serve the same purpose as the windmill in Ref. [15], as both are set in motion by local flow of the bulk gas.

2.2 Gas Flow and Temperature Gradients

Transport processes in gas are classified into flow regimes, distinguished according to the dimensionless Knudsen number, Kn . The Knudsen number is the ratio of the mean free path λ to a characteristic scale length L , and its value indicates the importance of molecular collisions. Thermal creep flow (TCF) is most prominent in the *slip-flow regime* ($10^{-3} < Kn < 0.1$), where, due to the dominance of collisions, the gas can be treated as an infinitely divisible fluid, but only with appropriate boundary conditions. By performing the experiment under vacuum

conditions, with surfaces at a centimeter length scale, it is assured that gas flow is in the slip-flow regime.

Thermal creep gas flow results from a non-uniformly heated gas being in contact with a solid surface. A temperature gradient with a component tangential to the surface drives a gas flow. The flow velocity is directed toward hotter gas regions and is largest at the gas-surface interface. In this way, TCF is a *boundary* effect.

The TCF effect depends strongly on the Knudsen number. In the slip-flow regime, where TCF is most important, the TCF gas flow velocity, tangential to the boundary at the boundary surface, is [28] $v_{creep} = b(2k_B T/m)^{1/2} Kn_T$. This is valid within a distance λ of the boundary, and not in the bulk gas. Here, b is a constant of order unity, k_B is Boltzmann's constant, T is the gas absolute temperature, and m is gas atom mass. Note that v_{creep} is proportional to the Knudsen number on the scale of the gas temperature gradient, Kn_T , revealing that TCF is more significant at larger mean free paths, or lower pressures, as was verified experimentally [15]. Here, $Kn_T \equiv (\lambda/T)(dT/dx)$, and (dT/dx) is the tangential component of the gas temperature gradient evaluated at the boundary.

Conditions that lead to TCF will often be accompanied by two other effects: a thermophoretic force and free convection. All three effects result from a temperature gradient. To design an experiment that allows distinguishing these effects requires careful planning. I next review the thermophoretic force and free convection, before presenting the design of my experiment.

The thermophoretic force \vec{F}_{th} arises when a small dust particle (usually microns or smaller in size) is exposed to a non-uniformly heated gas. Dust particles are pushed toward colder gas regions. This happens because a gas temperature gradient causes an anisotropy in the gas velocity distribution function, which in turn causes more momentum to be imparted to dust from hot gas regions than from cold gas

regions [29]. For a spherical particle in an unequally heated background of argon gas [9], $\vec{F}_{th} = 3.33(R^2/\sigma)k_B(-\vec{\nabla}T)$, where R is the dust particle's radius and σ is the collision cross-section for argon atoms. Note that unlike TCF, the thermophoretic force does not require a boundary, and it does not necessarily involve a gas flow. It involves a gradient of the gas temperature in a volume of gas, while TCF involves a tangential temperature gradient on a boundary.

Free convection is a gas flow driven by buoyancy when there is a temperature gradient. It requires a body force, such as gravity, that is aligned with the temperature gradient. Gravity, in combination with gas density gradients that arise from temperature gradients, leads to the gas flow. Hotter gas regions expand and rise, where they are then cooled. Colder gas regions condense and fall, where they are then heated. Free convection is often characterized by the dimensionless Rayleigh number \mathfrak{R} , which is generally interpreted as the ratio between buoyancy forces and diffusion forces. If a horizontal layer of fluid with vertical thickness h extends over a temperature difference ΔT , the Rayleigh number is $\mathfrak{R} = \frac{\Delta T g h^3 / T}{\nu \alpha}$ where ν is the fluid's kinematic viscosity and α is its thermal diffusivity [30]. Above a critical value \mathfrak{R}_{cr} , the fluid becomes unstable and free convection is important.

2.3 Experimental Design

The experiment is designed to detect TCF, and to isolate its effects. A *locally heated* solid boundary causes temperature gradients that drive gas flow. Dust particles serve as indicators of gas flow.

The design of the experiment isolates TCF from most other processes, except for the thermophoretic force and free convection. Thus, the experimental design allows me to conclude that I have detected TCF if it can be distinguished from the thermophoretic force and free convection. The thermophoretic force has a signature that is different from that of TCF, as is explained in detail later. Free convection is

ruled out two ways: a theoretical argument based on the Rayleigh number for the experimental conditions, and by comparing the horizontal and vertical dust kinetic energy in the experimental data.

My experiment's design is now compared to that of Ref. [17]. Both experiments isolate the effect of TCF, and enable detecting very slow gas flow by avoiding vertical dust sedimentation. My heat source is designed to drive TCF mostly *perpendicular* to gravity. Because my heat source is *independent* of the forces that confine dust, the effect of gas flow driven by TCF is then very clear since it disturbs the equilibrium; the effect can be turned on and off. In Ref. [17], bulk gas flow driven by TCF is aligned *anti-parallel* to gravity and also contributes to dust confinement. The design of their experiment allowed for calculation of the *gas flow* velocity field, as well as comparison to theory.

2.3.1 Apparatus

The apparatus makes use of a radio-frequency (rf) gas discharge plasma in a vacuum chamber. Polymer microspheres (dust particles) are injected [31], become electrically charged, and are levitated as a spherically-shaped suspension called a Coulomb ball or Yukawa ball [32]. This suspension is confined in equilibrium within the volume of a glass box. This equilibrium is purposely disturbed by *locally* heating the glass box to drive TCF, as described later.

The Yukawa ball's equilibrium is maintained by a configuration of forces. In the vertical direction, the electric force and a thermophoretic force balance gravity and ion drag. In the horizontal direction, the electric force balances interparticle repulsion between negatively-charged dust particles. The electric force is set up by applying a rf voltage (13.6 MHz, 72 V_{pp}) to the lower electrode. The upward thermophoretic force is set up by *uniformly* heating this lower electrode to a temperature of 70 °C.

The glass box plays two roles. First, it serves as a boundary that is heated using a laser. Second, the glass box provides horizontal confinement of the dust suspension, because the dielectric walls of the box modify the plasma's natural electric field [10]. The glass box rests atop the lower electrode, is open on top and bottom, and partially encloses a volume of $(40 \text{ mm})^3$ as in Fig. 2.1(a). The box is constructed from four glass plates ($40 \text{ mm} \times 40 \text{ mm} \times 1.5 \text{ mm}$) that are glued together at their edges.

There are a few required conditions to be met in order to observe TCF in dusty plasma. First, TCF is most readily observed in the slip-flow regime. Second, TCF requires a gas temperature gradient tangential to a solid surface. Finally, the flow of gas must be detectable, which can be difficult because it is a low Mach number flow. Next, I describe how the design of this experiment meets these conditions.

The parameters for the gas and the glass box assure me that gas flow inside the box is in the slip-flow regime. I used argon at 0.4 Torr ($1 \text{ atm} = 760 \text{ Torr}$), corresponding to $\lambda = 0.12 \text{ mm}$. For the box with $L = 40 \text{ mm}$, I find $Kn = 0.003$, which is at the lower limit for the slip-flow regime.

2.3.2 Localized heating

To detect TCF in isolation from other effects, it is desirable to have a heat source that does not disturb the electrical configuration of the plasma. As an optical solution, I used a 3-W 532-nm steady-state laser beam to *locally* heat two sides the glass box. The box absorbs some of the laser radiation. The laser is useful for heating glass, but not powerful enough to cause significant laser-plasma interactions with electrons and ions.

It is desirable for the temperature gradients due to laser heating to be mostly in the *horizontal* plane, for two reasons. First, forces that confine dust in equilibrium are weaker in the horizontal direction, as compared to the vertical direction. Thus,

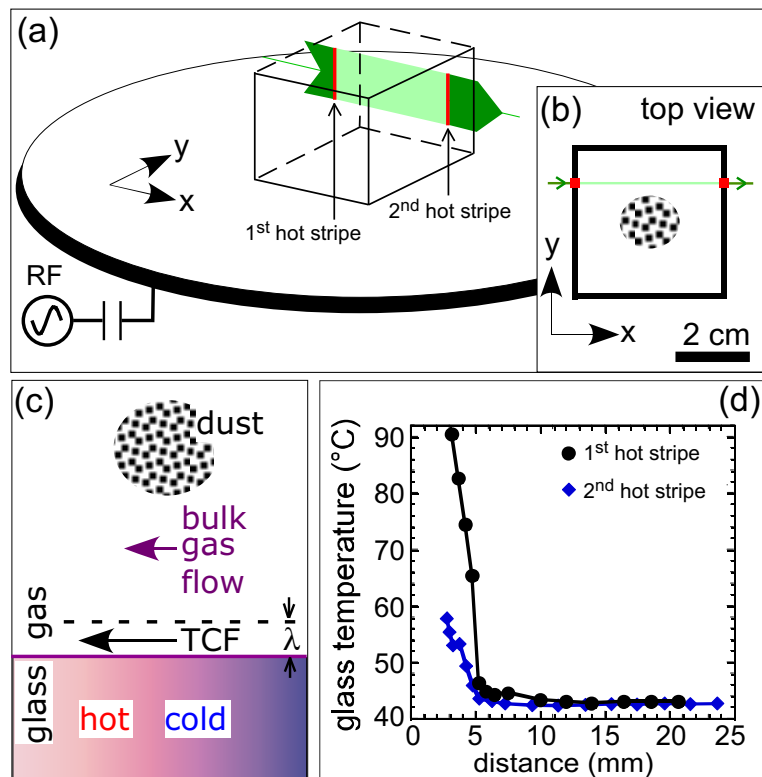


Figure 2.1: Laser heating a glass surface and driving a gas flow. A green vertical laser sheet is used to heat two stripes on a glass box, as illustrated from the (a) perspective view (dust not shown) and (b) top view (dust shown). The laser sheet strikes two faces of the box, creating two heated stripes (shown in red and indicated with two arrows), but does not strike dust. The laser sheet is shown both in the interior (light green) and exterior (dark green) of the box. (c) Sketch of gas flow arising from tangential temperature gradients at a glass-gas boundary. In the rarefied gas near the boundary, TCF occurs; this couples to the bulk gas farther from the boundary, causing it to flow also. Flow of the bulk gas disturbs the dust suspension, which is imaged. (d) Glass temperature, measured under the same vacuum conditions but without plasma, *vs.* horizontal distance from each of two heated stripes.

additional forces that *disturb* dust equilibrium (including \vec{F}_{th} and gas drag) have the greatest effect on a dust particle if they are directed horizontally. Second, driving dust motion horizontally helps distinguish TCF from free convection, which should effect dust motion mainly in the vertical plane.

To produce mostly *horizontal* temperature gradients, the laser beam is rastered [38] into a vertical sheet of laser light 16 mm high and 1 mm wide. It passes through two sides of the glass box, locally heating two stripes, as in Fig. 2.1(a) and 2.1(b). The laser is directed so that dust particles are not struck by the primary beam or any weaker reflected beams.

Since TCF is generated at boundaries, I identify the boundaries in the experiment that are heated. The glass box is *locally* heated in two vertical stripes. The only other nearby boundary is the lower electrode, which is large (17-cm diameter), and is *uniformly* heated. Thus, only the glass boundaries are expected to have a significant tangential temperature gradient, as required to drive TCF.

To clearly demonstrate the effect of the heat source, I performed two types of tests with dusty plasma, one using a heated box and the other using a control box. The heated box is made of common window glass, and it is heated by absorbing laser radiation. The control box (similar in size to the heated box) is made of fused silica, which has almost negligible absorption, so that it is not heated by laser radiation. All other conditions, including the ambient gas flow to the vacuum pump, are the same for the control. More detail is given in Sec. 2.4.1.

2.3.3 Detecting gas flow with dusty plasma

A suspension of microspheres in the dusty plasma is used to diagnose gas flow. My method of detecting TCF is to observe the motion of dust particles accelerated by flow of the bulk gas, which is driven by TCF at the boundary, as sketched in Fig. 2.1(c). To do this, I tracked the motion of individual dust particles by imaging

either a horizontal plane from above, or a vertical plane from the side. A digital camera was used to record movies at 53 frames per second. Micron-sized or larger particles are easiest to identify individually; here, I used 4.8- μm microspheres.

The method used here to detecting TCF differs from previous methods used in fluid mechanics experiments. Unlike in Ref. [15], where a windmill provided a single-point measurement of flow in a rarefied gas, here I use dust particles embedded in the gas to indicate gas motion everywhere within the volume of the dust suspension. This use of dust particles resembles velocimetry methods commonly used in fluid mechanics, except that in a plasma there are other vertical forces to offset gravity and avoid sedimentation.

To identify the effect of a drag force due to gas flow (driven by TCF or free convection) it must be distinguishable from the effect of the thermophoretic force \vec{F}_{th} , which inevitably will also occur. Here, a signature of a drag force is a steady-state flow of dust. Since $\vec{F}_{th} \propto \vec{\nabla}T$, it is a *conservative* force, and the work done by \vec{F}_{th} on a dust particle around a closed loop is $\oint \vec{F}_{th} \cdot d\vec{x} = 0$. Thus, \vec{F}_{th} cannot drive a steady-state flow of dust because it cannot add energy to the system. The drag force on a dust particle, however, is proportional to a velocity and is *nonconservative*, thus $\oint \vec{F}_{drag} \cdot d\vec{x} \neq 0$. A steady flow of gas can drive dust particles into a steady-state flow. In this experiment, I exploited this to distinguish the effects of a drag force from \vec{F}_{th} .

2.3.4 Temperature measurements

In a test with the same vacuum conditions mentioned above, but without plasma, I characterized the temperature gradients of the heated glass boundary. Using a thermocouple, I measured the *horizontal* profiles of glass temperature due to the laser heating two faces of the glass box. I did this by holding fixed the position of the thermocouple and varying the position of the laser beam (steered by adjusting

the orientation of a voltage-controlled mirror). The result is glass temperature plotted *vs.* distance from the heat source for each heated stripe, Fig. 2.1(d). The heating of the glass had a time scale of ≈ 60 s, during which most of the observed temperature increase occurred.

Knowing the temperature gradient allows me to estimate \vec{F}_{th} and v_{creep} . These quantities depend on temperature gradients at different locations: v_{creep} depends on the tangential component of the temperature gradient at the glass boundary while \vec{F}_{th} depends on the temperature gradient in the bulk gas, where dust particles are located. In Fig. 2.1(d), the temperature gradient varies from 16 K/mm at a distance of 4 mm from the heat source to 0.2 K/mm at 20 mm from the heat source. Using these measurements, the *horizontal* bulk gas temperature gradient is calculated as ≥ 0.2 K/mm (this should not be confused with the *vertical* temperature gradient which contributes to equilibrium). Using this value, it is estimated that \vec{F}_{th} on one particle due to laser heating is $\geq 1.2 \times 10^{-13}$ N. This is about one eighth the force of gravity, which is 8.6×10^{-13} N. Using the larger value for the temperature gradient, I predict v_{creep} near the heated glass to be ≤ 2 m/s.

2.4 Results

In excluding all alternative explanations for my results, other than TCF, my logic will have three steps. First, I will explain how the dust motion has been demonstrated to arise from temperature gradients. Second, I will explain how the stirring motion of dust must be due to a coupling between dust and a flow of gas (not \vec{F}_{th}). Third, I will eliminate free convection as a possibility, leaving TCF as the only explanation for the results.

2.4.1 Plasma effects vs temperature gradients

In the main experiment with plasma, I first compare results of tests with the heated and control boxes (Fig. 2.2). In each test, as explained in Sec. 2.3, a dusty plasma (Yukawa ball) is confined within the volume of the glass box. A single laser strikes two faces of the glass box, as in Fig. 2.1, and any resulting dust motion is monitored from above. Any differences in the results for the two tests must be attributed to heat due to laser-light absorption in the common window glass of the heated box. Plasma forces such as the electric force and the ion drag force cannot be responsible because the plasma's electrical conditions are not altered by the laser heating. Because the laser never directly strikes dust, there is no radiation pressure force affecting dust motion. The force of gravity acts perpendicular to the horizontal viewing plane. Finally, any gas drag force due to ambient gas flow to the vacuum's pump is the same for the heated and control boxes.

Results shown in Fig. 2.2 and 2.3 establish that a temperature gradient drastically disturbs the Yukawa ball. Particle positions before laser application (blue circles) and during laser application (red squares) are shown in Fig. 2.2, for tests using both the heated box and the control box. While the Yukawa ball in the control box showed no change when the laser beam was applied (Fig. 2.2(b)), the Yukawa ball in the heated box changed in two ways: it was displaced and it rotated. In Fig. 2.2(a), the suspension is displaced away from the heat source by a distance of about 6 mm, which is over half the size of the Yukawa ball. The steady-state flow of dust for the test using a heated box is shown in Fig. 2.3, with arrows indicating dust velocity and a color map indicating dust vorticity. The suspension rotates into a steady state, as if being *stirred*, with the fastest particles at the edge and slower particles in the interior. Thus, it is concluded that the dust motion that ensues when the laser strikes the box is attributed to resulting gas temperature gradients

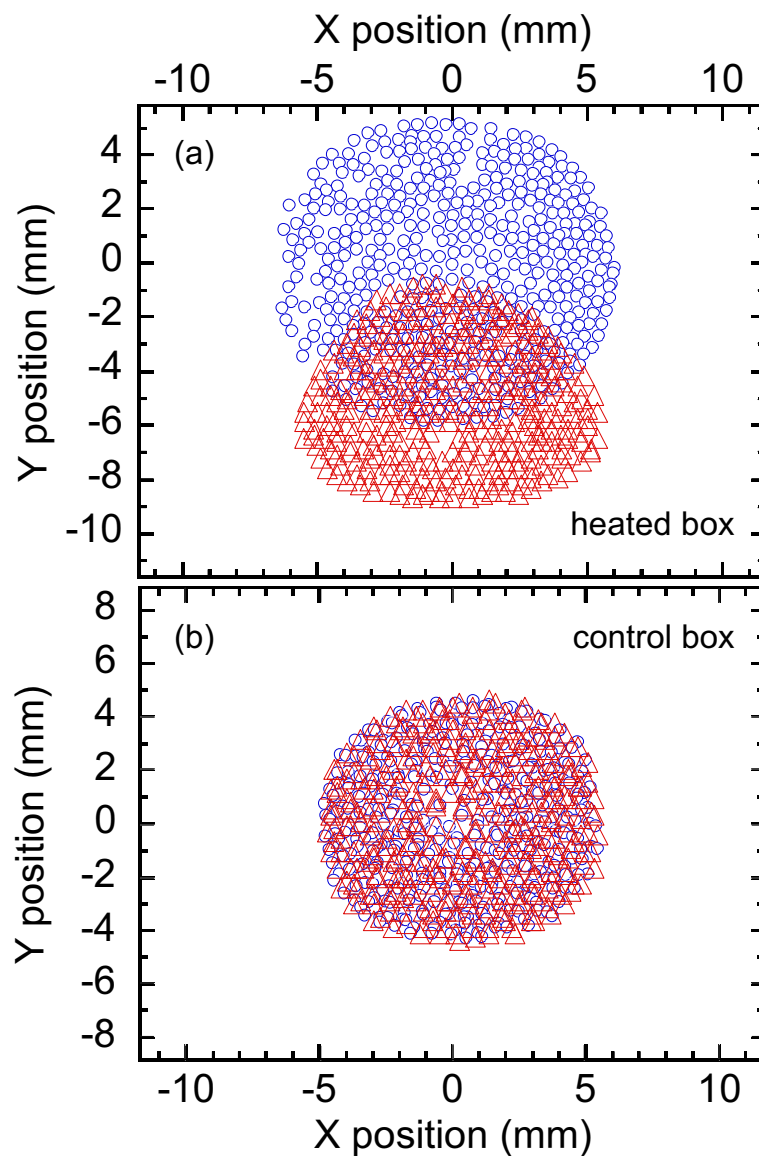


Figure 2.2: Top view of dust particle positions, from separate tests using (a) the heated box that absorbs light and (b) the control box that does not absorb light. Each panel shows dust particle positions in a horizontal plane before laser application (blue circles) and during laser application (red triangles). The origin is the horizontal center of the glass box. A laser sheet strikes the two faces of the box, as in Fig. 2.1(a) and 2.1(b). In the test with the heated box, the dust suspension (Yukawa ball) is *displaced* away from the heating laser beam to a new *horizontal* equilibrium position. This displacement is attributed to the thermophoretic force.

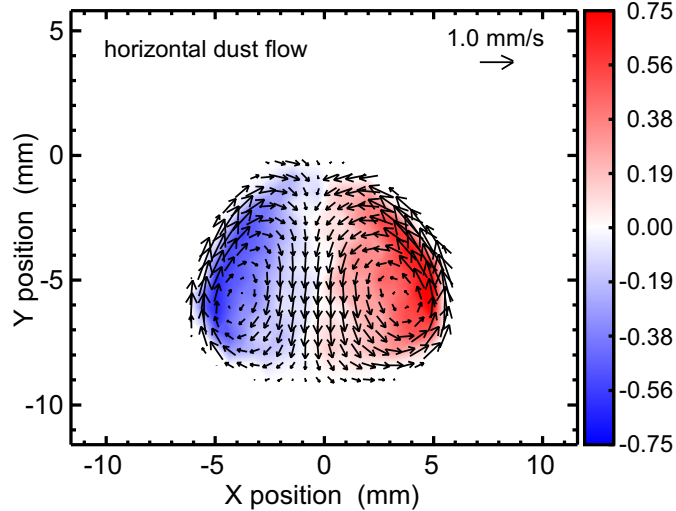


Figure 2.3: Top view of the steady-state dust velocity field \vec{V} (black arrows) and vorticity $\vec{\nabla} \times \vec{V}$ (color map) in units of s^{-1} . Gravity is into the page. The origin is the equilibrium center of the Yukawa ball. Data shown are dust velocities mapped to a regular grid (40×30), and averaged over the movie's last 100 frames (2 s). The stirring of dust into a horizontal flow is the main result that I seek to explain.

and not to any plasma forces.

2.4.2 Thermophoretic force vs gas drag force

The displacement of the Yukawa ball is due to \vec{F}_{th} . Dust is pushed away from the heat source toward colder gas regions, consistent with the direction of \vec{F}_{th} . The estimate above for the magnitude of \vec{F}_{th} is large enough to account for the Yukawa ball's displacement, based on the force calculations of Arp *et al.* [10].

The steady-state rotational flow of dust particles is due to coupling between dust and a flow of gas, or gas drag. The observation of a steady-state flow (shown in Fig. 2.3) is a signature that rules out \vec{F}_{th} , as argued in Sec. 2.3.3, based on the conservative nature of \vec{F}_{th} . Thus, while I do observe effects of \vec{F}_{th} (dust particle displacement), it cannot account for the stirring of dust particles. Gas flow is the only explanation for dust stirring.

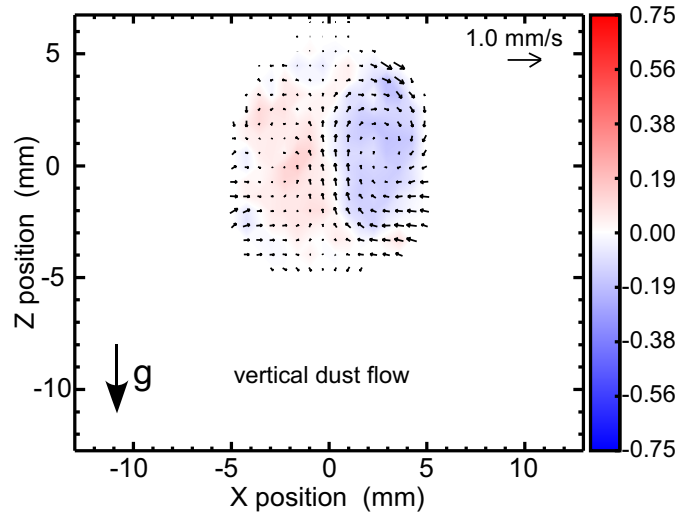


Figure 2.4: Side view of the steady-state dust velocity field \vec{V} (black arrows) and vorticity $\vec{\nabla} \times \vec{V}$ (color map) in units of s^{-1} . Gravity is directed downward. The origin is the equilibrium center of the Yukawa ball. Data shown are averaged and scaled as in Fig. 2.3. Comparing to Fig. 2.3 shows that the flow of dust is predominantly horizontal, indicating that the flow of bulk gas is also predominantly horizontal.

2.4.3 Thermal creep flow vs. free convection

At this point, it has been demonstrated that the stirring motion of the dust is due not to plasma effects but rather to temperature effects, and the thermophoretic force has been eliminated as a candidate for explaining the stirring. The two effects that remain to consider are TCF at the glass boundary and vertical free convection due to gas buoyancy.

Next, free convection is eliminated as an explanation for the stirring observations, for two reasons. First, I estimate the Rayleigh number and find that it is much too low for free convection. Second, I compare the dust kinetic energies associated with horizontal and vertical motion. Vertical motion is of interest for free convection, because buoyancy drives vertical motion, which can then couple to

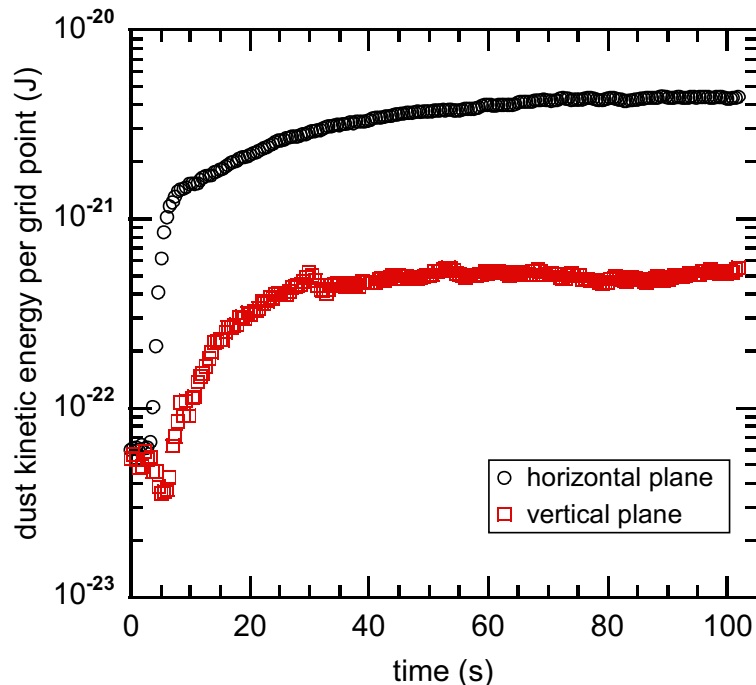


Figure 2.5: Time series of kinetic energy of dust particles in a horizontal plane averaged over five runs (black circles) and of particles in a vertical plane averaged over two runs (red squares). The laser heating is applied at $t = 5$ s. Dust motion in the vertical direction is much weaker than in the horizontal. The comparison of vertical *vs.* horizontal motion here and in Fig. 2.4 leads me to eliminate free convection as the cause of the observed stirring in Fig. 2.3. Each datum is averaged over all non-zero gridpoints in the 40×30 field of view and then over 100 contiguous frames (2 seconds).

horizontal motion.

First, I compare the Rayleigh number \mathfrak{R} in our experiment to the critical Rayleigh number \mathfrak{R}_{cr} for the onset of buoyancy-driven flow (free convection). For the experimental conditions used here, I estimate $\mathfrak{R} < 0.1$. This is much lower than $\mathfrak{R}_{cr} = 1708$, above which free convection becomes important [30, 34]. Thus, I suspect that free convection is not significant in this experiment.

Second, I compare horizontal and vertical dust motion. To do this, I observed dust motion from both the top and the side, using the same camera in separate runs.

The steady-state dust velocity map in the *horizontal* plane is shown in Fig. 2.3. For comparison, the steady-state dust velocity map in the *vertical* plane is shown in Fig. 2.4. In order to compare scalar quantities, I compared the kinetic energy associated with horizontal velocity components to the kinetic energy associated with vertical velocity components. I performed five runs viewing from the top, and two from the side. All runs showed a clear increase in dust kinetic energy that coincided with the onset of laser heating, and eventually reached a steady-state energy. For both horizontal and vertical motion, there was a slight variation in the steady-state energy from run to run. The average steady-state energy for *horizontal* motion for five runs was $(4.4 \pm 1.4) \times 10^{-21}$ J, while the average steady-state energy for *vertical* motion for two runs was $(5.3 \pm 1.3) \times 10^{-22}$ J. The time series for these kinetic energies is shown in Fig. 2.5, with black circles showing energy in the horizontal plane and red squares showing energy in the vertical plane. Laser heating begins at $t = 5$ s, and remains on for the remainder of the time series. At all times after heating began, kinetic energy associated with vertical motion was nearly a factor of ten less than horizontal motion. Dust energy reaches a steady-state about 1 minute after laser heating begins, the same as the time scale for laser heating, as mentioned in Sec. 2.3.4.

It is concluded that steady-state stirring of the dust suspension is not due to free convection, leaving TCF as the only explanation. I know that the gas flow is not driven by free convection, because horizontal dust motion had nearly a factor of ten more energy than vertical motion, as shown in Fig. 2.5. This is further supported by the earlier estimate for the Rayleigh number.

2.5 Summary

I performed an experiment with a dusty plasma that was designed to observe TCF, in isolation from other effects, as described in Sec. 2.3. A stirring motion was

observed in the confined dust suspension. This stirring motion developed as two glass boundaries heated up, due to applying a laser beam. In Sec. 2.4, I presented logic to dismiss, in three steps, all alternative effects that might account for our observations of stirring. First, a test with a control box allowed me to exclude from consideration all plasma-related forces that are not associated with temperature gradients. Second, by noting that stirring motion requires a nonconservative force, I eliminated the thermophoretic force as an explanation. Third, I eliminated free convection two ways: finding that the Rayleigh number was much too small, and by comparing the vertical and horizontal motion. I therefore conclude that the stirring motion observed results from the flow of bulk gas, which is driven at the boundaries by TCF.

This experimental test serves two purposes, for two different scientific communities. For the fluid mechanics community, it serves as a rare experimental verification of the existence of TCF. For the plasma physics community, it verifies the recently reported demonstration [17] that TCF can have a significant effect on dusty plasmas. The experiment here differs from the one used in Ref. [17] in several ways, including the configuration design so that TCF results in a horizontal flow to allow distinguishing it from convection, and an optical method of heating a boundary.

CHAPTER 3

OBSERVATION OF THE SPATIAL GROWTH OF SELF-EXCITED DUST-DENSITY WAVES

3.1 Introduction

Dusty plasma is a suspension of small (micron-size) dust particles in a plasma background (electrons, ions, and neutral gas). In the laboratory, the dust becomes negatively charged by absorbing electrons and ions, and are levitated in the plasma sheath's strong electric field. Due to their large mass m_d , dust particles have a much smaller charge-to-mass ratio than electrons and ions. Thus, the time scales of dust dynamics are comparatively much longer, and easily observed.

If a dust particle's Coulomb potential energy is larger than its kinetic energy, the dusty plasma is said to be “strongly coupled.” In a strongly-coupled dusty plasma, the dust particles cannot easily move past one another. Instead, they organize themselves in a structure that is similar to atoms in a solid or a liquid. Due to the dust particle's large negative charge ($Q_d = -eZ_d$), mutual dust repulsion dominates their dynamics. In contrast, most electron and ion plasmas are “weakly coupled.” With weak coupling, charged particles move easily past one another, like atoms in a gas. In many dusty plasma experiments, the charged dust particles are strongly coupled amongst themselves, but the electrons and ions are weakly coupled.

Dusty plasma exhibits waves that can be easily observed. Dust motion can be directly imaged with cameras. Dusty plasma is a medium that can support both compressional [35, 36] and shear (transverse) waves [37, 38]. Waves can be externally excited by electrical [39] or optical manipulation [37, 35, 38, 36]. They have a natural phonon spectrum due to random thermal motion [40]. Finally, coherent waves can be excited naturally (i.e., self-excited). The most common example is the dust-acoustic wave [41, 42], also called the dust-density wave.

The dust-density wave (DDW) is a low-frequency compressional wave that propagates in dusty plasma [43], where dust particles participate directly in the wave dynamics. The charged dust particles are a fluctuating space charge, and are shielded from each other by the electrons and ions. However, the shielding is incomplete and there is a slight misbalance in charge neutrality, which sets up the wave's electric field. This electric field provides the dust particles' restoring force for the wave. Experimental studies of the DDW have been performed using a variety of plasmas, both in the laboratory [44, 45, 46, 47, 48, 49, 50, 51, 52] and under microgravity conditions [53, 54, 55]. The DDW frequency is usually near or below the dust plasma frequency ω_{pd} , which is defined by $\omega_{pd}^2 \equiv n_d e^2 Z_d^2 / m_d \epsilon_0$ where n_d is the average dust number density. Typical values for $\omega_{pd}/2\pi$ range from a few Hz to near 100 Hz.

The DDW will often self-excite due to an ion-flow instability. This has been observed both in ground-based experiments [44, 50, 51, 48] and under microgravity [54, 55]. The free energy available in the flowing ions [56] can drive the DDW to large amplitudes, leading to nonlinear effects [48, 50, 51, 52].

The ion-flow instability must compete with dissipation due to neutral gas drag. The wave can be completely damped out at sufficiently high gas pressures, typically about 1 Torr (1 atm = 760 Torr). The typical time scale for the damping of dust motion by neutral gas collisions is the Epstein collision rate ν_{dn} , which is defined by $\vec{F}_{drag} \equiv -m_d \nu_{dn} \vec{V}_d$, where \vec{F}_{drag} is the drag force experienced by dust due to gas [57] and \vec{V}_d is the relative velocity between dust and gas. For typical micron-size polymer dust particles at a gas pressure of 1 Torr, ν_{dn} is about 100 s^{-1} , which is comparable to a typical dust plasma frequency.

The balance between the ion-flow instability and gas damping determines an instability threshold. This threshold occurs at a critical gas pressure. At the

threshold, lowering the gas pressure (or increasing the ion flow) will cause the wave's onset and subsequent growth, while raising the gas pressure will suppress wave excitation. The instability threshold has been studied previously in experiments [50, 58] and theory [56]. Below the critical gas pressure, a linear growth of the DDW is predicted.

I know of three previous reports of DDW growth rate measurements. In one case [59], singular-value decomposition was used to measure the amplitude profile. In two other cases, the spatial variation of dust density [49] or velocity [60] was fit to an oscillating function with an exponential profile. However, I do not know of any previous measurements of DDW growth rate near the instability threshold. This lack of previous measurements suggests a need to develop a suitable experimental procedure, which I do here.

Here, I report experiments carried out near the critical gas pressure. Using a dust cloud suspended in the sheath of an rf plasma, I reduce the gas pressure in small steps. Depending on the gas pressure, waves naturally excite and grow as they propagate downward through the dust cloud.

As the main result of this chapter, I report growth rate measurements for self-excited dust-density waves. The wave's growth rate is measured for a range of gas pressures near and below the critical gas pressure. This is done using a phase-sensitive analysis method to quantify the wave's amplitude and phase as a function of height in the dust cloud. I find that the growth rate increases as gas pressure decreases. At the lower pressures, the wave amplitude grows faster, eventually reaching a nonlinear amplitude saturation as it traverses the dust cloud.

Additionally, experimental results are compared to a linear dispersion relation that assumes three fluid components (electrons, ions, and dust). The fluid model has been adapted to account for strong coupling amongst dust particles.

3.2 Experimental Design

This experiment is designed to observe the growth of self-excited dust-density waves propagating in a strongly-coupled dusty plasma. A quantity of about 10^5 polymer dust particles (diameter $4.8 \mu\text{m}$, mass density 1510 kg/m^3 , melamine-formaldehyde) are introduced into an argon plasma using a dust dispenser that is similar to a salt shaker with a single hole. The dust particles are trapped in the plasma within the volume of a glass box (fused silica glass, as in Ch. 2). The box has dimensions of $3 \text{ cm} \times 3 \text{ cm} \times 3 \text{ cm}$, is open on top and bottom, and rests on an electrode, as sketched in Fig. 3.1. The electrode is capacitively coupled and powered at radio frequency (13.6 MHz) with a voltage of $85 V_{\text{pp}}$, which sustains the plasma through electron-impact ionization. (In contrast to the experiment in Ch. 2, the electrode is not actively heated, so there is no thermophoretic force.) The dust particles are levitated in the plasma sheath, filling a volume near the bottom of the glass box. The sheath's vertical electric field E_z serves two purposes. First, the sheath electric field drives a strong downward ion flow, which is the DDW's instability energy source. Second, it provides an electric force that balances the dust particles against gravity. The walls of the vertical glass box modify the plasma's natural electric field, providing horizontal dust confinement [10]. This combination of forces confines the dust cloud so that it has many horizontal layers, with overall dimensions of about 22-mm width and 5-mm height.

The dust cloud is illuminated with a vertical laser sheet and is imaged with a digital video camera that views from the side, as sketched in Fig. 3.1. The camera records images at 500 frames per second at a spatial resolution of $R = 76.4 \text{ pixels/mm}$.

The primary observable in this experiment is dust number density, which is derived from the recorded video images. Regions with higher dust number density

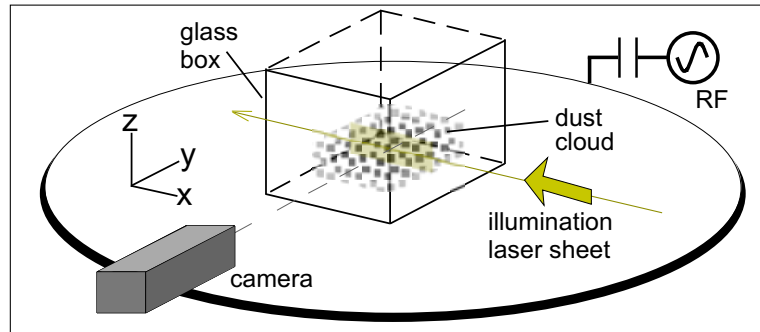


Figure 3.1: Sketch of the experimental setup. In a radio-frequency argon plasma, dust particles are levitated within the volume of a glass box, forming a dusty plasma. A laser sheet illuminates dust in a vertical plane and the dust cloud is imaged from the side with a digital video camera. For each movie, images are recorded at 500 frames per second for 2.048 seconds.

scatter more laser light. I verified that the image intensity is linear with dust number density by checking that the camera has a linear response with no offset, and by noting that the dust cloud is optically thin (laser light scattered from dust particles is not rescattered in other regions of the dust cloud).

The imaging setup is designed to detect small variations in dust number density. To reduce the DDW detection threshold, I selected a low-noise 12-bit camera that subtracts background noise levels. Also, I operated the illumination laser at the highest power that would not visibly disturb the dust particles, 0.85 W distributed over a 4-cm high laser sheet.

The experiment begins with a dust cloud levitated in a plasma at a gas pressure of 426 mTorr, which is just high enough that the DDW is not observed. In other words, at the starting pressure the dust cloud is stable. The stable dust cloud's central region is shown in the side view image in Fig. 3.2(a). Bright spots are individual dust particles. The stable dust cloud is a highly-structured strongly-coupled dusty plasma. It has many horizontal layers, which are planes of a simple hexagonal lattice, with a vertical alignment of dust due to ion flow [61].

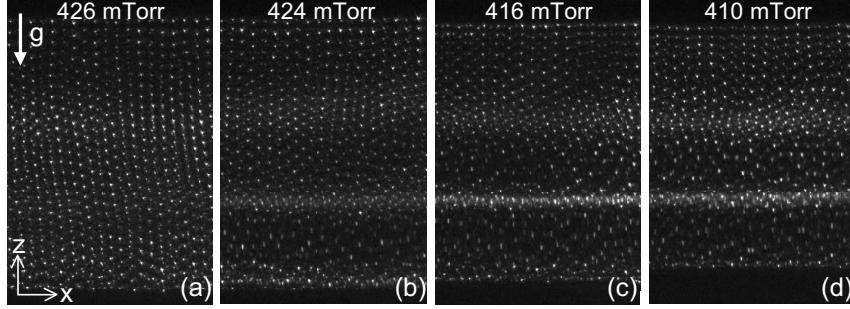


Figure 3.2: Single side view images of the dust cloud’s central region. Bright spots are individual dust particles. Depending on the gas pressure, energy from a downward ion flow can couple to dust motion, causing nearly planar compressional waves to be excited and propagate in the $-\hat{z}$ direction. (a) At the starting pressure of 426 mTorr, no wave is observed. Under these stable conditions, dust particles are mainly arranged in horizontal layers. (b) Near a critical pressure of 424 mTorr the effect of ion flow barely overcomes gas damping, and a small amplitude wave grows as it propagates downward. The wave fronts are visible in the still image. (c) and (d) At lower pressures, ion flow more effectively couples to dust motion, and the wave grows at a faster rate, reaching larger amplitudes. Each panel shows the same $3.57 \text{ mm} \times 5.29 \text{ mm}$ spatial region. Gravity is downward.

Starting near the instability threshold, the instability can be induced by either an increase in ion flow or a decrease in gas damping (pressure), resulting in a DDW. Unlike the ion flow, which is difficult to establish at a desired level because it depends on the plasma conditions, the gas pressure is easily controlled by the experimenter. Thus, I choose to vary the gas pressure. The critical gas pressure corresponds to the instability threshold, and will vary depending on plasma parameters, dust density, and the size of the dust cloud.

To observe wave growth in the dust cloud near the instability threshold, I make observations at a series of gas pressures p that are decreased in steps. In each step, I wait about 1 minute to assure that the gas pressure and dust cloud has reached steady conditions. Then, under steady conditions, I record a 1024-frame movie, with a duration of 2 s. Each movie corresponds to one pressure. The steps in gas pressure are in 2 mTorr intervals, which I choose to provide a fine resolution

near the instability threshold. Planar wave fronts are observed for pressures ranging from the critical pressure down to 404 mTorr, and it is for this range that I recorded data.

3.3 Observations

A self-excited dust-density wave is observed propagating downward through the dust cloud, as seen in the still images of Fig. 3.2. The wave is not spatially uniform, but grows in amplitude as it traverses the dust cloud in the $-\hat{z}$ direction. In Sec. 3.5, I report measurements of the wave's growth rate.

The wave fronts are nearly planar, which will be important in subsequent analysis. The wave fronts are especially planar in the region that is analyzed, shown in the panels of Fig. 3.2. Within this analyzed region, the variation across the horizontal x coordinate of the wave front's vertical position is less than 1% of the wavelength. In other words, the wave front has very little curvature. Outside of the analyzed region, the wave fronts have a slight upward curvature, as can be seen in Fig. 3.3.

A critical gas pressure of 424 mTorr was observed for the dust cloud. The critical gas pressure was quantified by varying the pressure and finding that a DDW was detectable at 424 mTorr, but not at 426 mTorr. The wave was detected by viewing the movies and by using the image analysis methods described later in Sec. 3.4. I will use the term *observed* critical gas pressure because its measurement is limited by the detection threshold of the imaging. If there were no instrumental limitations, then the measured critical gas pressure would be presumably somewhat higher.

A single cropped video frame of the DDW at 424 mTorr is shown in Fig. 3.2(b). In the upper portion of the cloud, the amplitude of this compressional wave is small enough that individual particles are still easily resolved. As the DDW propagates

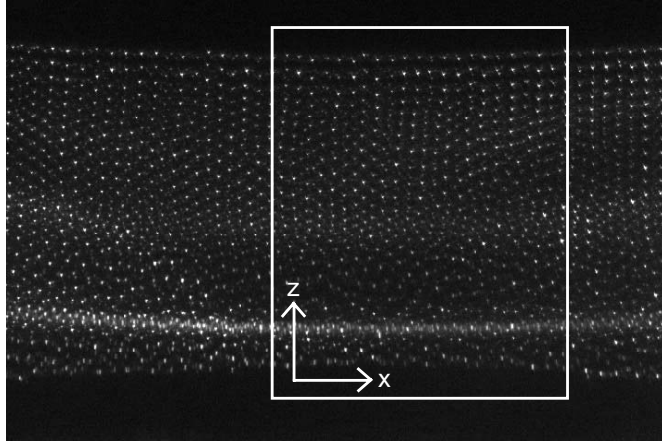


Figure 3.3: Image showing the DDW propagating downward through the dust cloud at the critical gas pressure of 424 mTorr. The white rectangle indicates the spatial region that is analyzed. It is the same region that is shown in each panel in Fig. 3.2. Within this region, the wave fronts are sufficiently planar to justify a one-dimensional analysis.

downward, the wave amplitude grows. In the lower portion, the bright horizontal stripe corresponds to a high-density wave front. There, dust compression is large enough to obscure the particle discreteness.

Reducing the gas pressure further leads to a greater wave amplitude. This trend is shown in the image panels in Fig. 3.2(c)-(e). Each panel shows a cropped image from a movie recorded at a different gas pressure. The dust number density, as indicated by image brightness, reaches its greatest values in the wave fronts at lower gas pressures. Next, I develop a quantitative amplitude analysis method, which is used to measure the wave's spatial growth rate.

3.4 Analysis

In this analysis, only collective wave properties are considered, and not individual dust particle dynamics. However, the analysis starts with the recorded video images. Instead of tracking the motion of individual dust particles, as is done in some dusty plasma experiments using video microscopy [61], here only the image

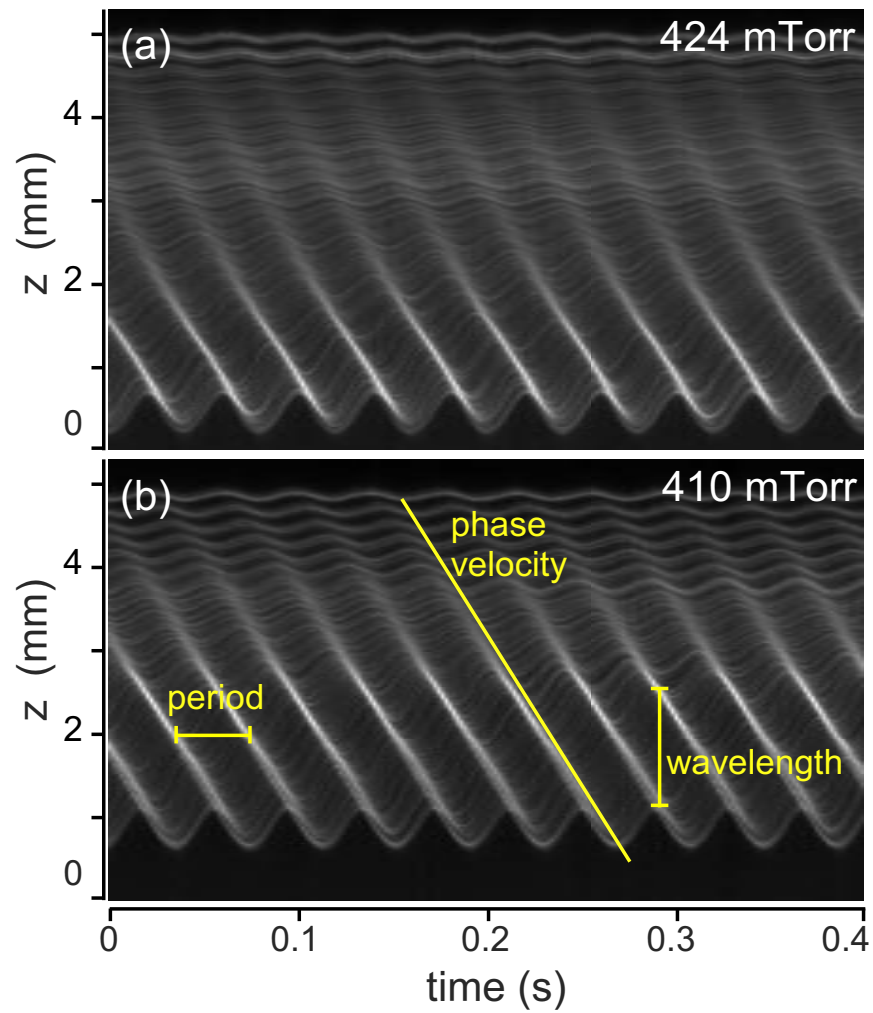


Figure 3.4: Portions of space-time diagrams for pressures (a) 424 mTorr and (b) 410 mTorr. Gray scale maps like these are the basis for all my analysis. The bright equally-spaced sloped lines indicate wavefronts. Amplitudes grow as the wave propagates downward.

intensity is used. Particle discreteness is ignored.

3.4.1 Space-time diagrams

For each movie, the basis for the analysis is the space-time diagram, which is a 2D gray scale plot of image intensity. As explained in Sec. 3.2, the image intensity is proportional to dust number density. In a space-time diagram, the vertical axis is vertical position z , and the horizontal axis is time t .

A space-time diagram is constructed from recorded images, such as those shown in Fig. 3.2, as follows. First, each movie frame is cropped to the same spatial region (273 pixels \times 404 pixels), which is indicated by the rectangle in Fig. 3.3. Since the wave fronts are nearly planar, especially in the analyzed region, the dust number density varies only with the z coordinate. Second, image intensities are averaged over the ignorable horizontal coordinate x , yielding data for intensities as a function of z (i.e., a vertical profile of intensity). These profiles are produced for each frame (i.e., each time t that an image was recorded). Finally, profiles from each frame are stacked side-by-side, to yield a space-time diagram with time varying on the horizontal axis.

The space-time diagram provides a visual indication of the propagating wave. Wave fronts appear as a sequence of bright and dark stripes. Examples are shown in Fig. 3.4 for gas pressures of 424 mTorr and 410 mTorr, and are similar to data at other gas pressures.

In this experiment, the waves are extremely coherent and periodic. This coherency allows for identifying the period, phase velocity, and even wave growth. Phase velocity is indicated by the slope of the stripes. Amplitude is indicated by the magnitude of the temporal intensity variations. The dominant frequency of the waves is easily quantified as the inverse of the period between stripes, as indicated

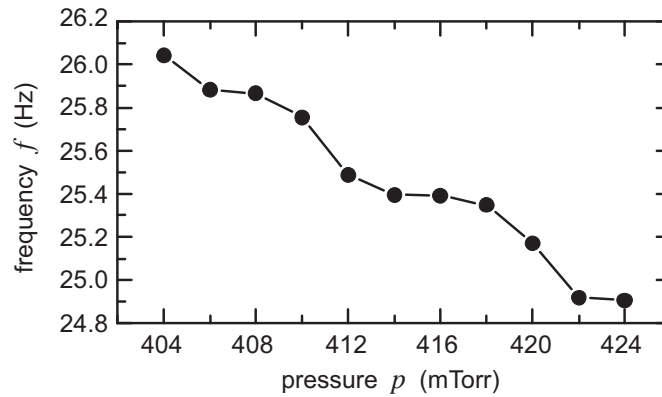


Figure 3.5: The dominant frequency f exhibits a slight downward trend with gas pressure. The data points shown are the result of calculating the power spectrum of the space-time diagram.

in Fig. 3.4(b).

3.4.2 Dominant frequency

For the design of this experiment, wave energy is largely concentrated in one dominant frequency f . As an example, for $z > 2$ mm at a pressure of 424 mTorr, over 90% of the wave energy is concentrated in a very narrow bandwidth around f , with all other energy at its harmonics.

The dominant frequency f changes only slightly with gas pressure. As gas pressure decreases from 424 to 404 mTorr, f ranges between 24.9 and 26.0 Hz, as shown in Fig 3.5.

Unlike some other experiments [62], here the wave frequency is nearly independent of position in the dust cloud. The dominant frequency f does not vary measurably with z . The spatial invariance of f is true for all gas pressures reported here.

3.4.3 Amplitude and phase

To measure the growth of the wave, I developed (along with my advisor John Goree) an amplitude analysis method that is phase sensitive. The method is analogous to the principles of an electronic instrument called a lock-in amplifier [63]. This method yields the phase $\phi(z, t)$ and amplitude $A(z, t)$. This method requires that the frequency f be known, that it does not vary with position, and that it varies slowly or not at all with time. It also requires a planar wave. The DDW in this experiment satisfies these requirements.

In general, the amplitude analysis method begins by finding the frequency f , and then the following procedure yields the phase ϕ and the amplitude A . The procedure starts with a given waveform $D(\tau)$, which can be, for example, an intensity time series for a given position z in one of the space-time diagrams. The difference between $D(\tau)$ and its time-average $\langle D(\tau) \rangle$ is multiplied by a reference sine wave of frequency f with an adjustable phase β . This product is then averaged over N reference wave cycles,

$$I(\beta) = \frac{f}{N} \int_0^{N/f} (D(\tau) - \langle D(\tau) \rangle) \sin(2\pi f\tau - \beta) d\tau. \quad (3.1)$$

The resulting integral I depends on the adjustable phase β , which must now be selected. Next, β is varied to find the value β_{max} that maximizes $I(\beta)$. Finally, β_{max} is interpreted as the phase ϕ , and $I(\beta_{max})$ as the amplitude A .

In this experiment, the amplitude analysis method was applied to the intensity data in the space-time diagrams, yielding the amplitude $A(z, t)$ and phase $\phi(z, t)$. The inputs required for Eq. (3.1) are f , N , and $D(\tau)$. To determine the frequency f , I used a power spectrum of the space-time diagram. Each space-time diagram was partitioned into “sections” that are $M = 15$ pixels in vertical space and $N = 5$ wave periods in time. These sections define the spatial (M/R) and temporal resolution

(N/f) of the amplitude and phase results. Within each section, I averaged the M pixel intensities at each time, resulting in the time series $D(\tau)$.

Applying Eq. (3.1) to each section in a space-time diagram, yielded the full spatial and temporal dependence of the amplitude $A(z, t)$ and phase $\phi(z, t)$. The spatial profiles $A(z)$ and $\phi(z)$ were calculated by moving the partitioned section throughout the vertical extent of the dust cloud in one-pixel steps, calculating A and ϕ at each step. These spatial profile calculations were repeated at time intervals separated by the temporal resolution N/f . To choose a value for N , I require that N/f is at least as long as the time required for the wave to transit the entire dust cloud. For the experimental parameters used here, I chose $N = 5$, so that the time resolution was typically 0.2 s, and the movies of duration 2 s yielded ten spatial profiles. As expected in this experiment, I found that all ten of these profiles look alike, since the gas pressure and other conditions remained steady during each movie in this experiment. (This is in contrast to the experiment that will be presented in Ch. 4, where gas pressure changes during the recorded movie, and thus time dependence is important.)

3.5 Growth Rate Results

Spatial profiles of phase $\phi(z)$ and amplitude $A(z)$ are indicators of wave propagation and growth, respectively, and are shown in Fig. 3.6 for three different gas pressures. The phase ϕ varies linearly with z , indicating a propagating wave. The direction of wave propagation is downward, as indicated by a phase that increases as position z decreases, as shown in Fig. 3.6(a). The phase varies over about 6π radians, indicating that there are about 3 wavelengths in the vertical extent of the dust cloud. At small wave amplitudes near the top of the dust cloud (large z), there is some ripple in $\phi(z)$, which is an artifact of horizontal layering of dust.

As the DDW traverses the dust cloud, its amplitude grows exponentially with

a well-defined spatial growth rate. The growth rate k_i is measured by fitting the amplitude profile to an exponential. Semi-log plots of $A(z)$ along with their exponential fits are shown in Fig. 3.6(b). As an example, near the instability threshold at $p = 424$ mTorr, the slope of the dashed line in Fig. 3.6(b) gives a measured growth rate of 0.61 mm^{-1} . The wave amplitude grows exponentially throughout most of the dust cloud, but not all of it. The growth saturates, reaching a maximum amplitude in the lower region of the dust cloud. To avoid any effect of this saturation in the growth rate measurements, data was fit only up to 0.3 mm above the position of maximum amplitude.

There is no evidence of a reflected wave at the dust cloud's bottom edge, where the amplitude quickly drops. Reflected waves do not grow due to the instability, because they propagate in the opposite direction of the flowing ions. Instead, they are only damped by gas friction. Using the known Epstein collision rate ν_{dn} and the measured phase velocity v_{ph} of the downward-propagating wave, I estimate that the upward-propagating reflected wave would be completely damped out in a very short distance $v_{ph}/\nu_{dn} \approx 0.3$ mm, comparable to one or two dust particle spacings.

As the main result of this chapter, measurements indicate that the growth rate of the downward-propagating wave increases as the neutral gas pressure is decreased. All measured growth rates k_i are plotted as open circles vs. gas pressure p in Fig. 3.7(a). Regardless of how the DDW is theoretically modeled, this trend is expected. Reducing gas pressure tends to promote wave growth for two reasons. A lower gas pressure reduces neutral gas damping and it increases the ion flow velocity. The ion flow increases because mobility is inversely proportional to gas pressure.

All the growth rate results reported in Fig. 3.7(a) are for the dust cloud's upper region, where nonlinear effects are weak. As the wave traverses the dust cloud, the amplitude grows large and saturates in the dust cloud's lower region.

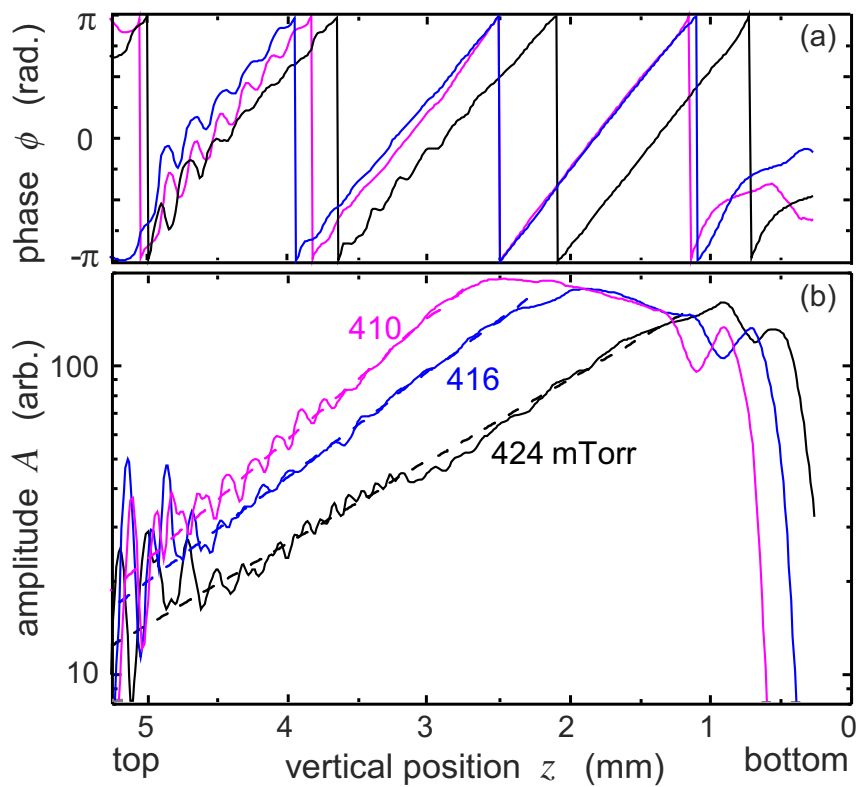


Figure 3.6: Spatial profiles of the dust-density wave's (a) phase $\phi(z)$ and (b) amplitude $A(z)$ for three gas pressures. These profiles are computed using the method described in Sec. 3.4.3. The growth is more rapid at lower gas pressures. Amplitude data (plotted log-linear) reveal exponential growth as the wave propagates downward. The growth rates are quantified by fitting the profiles to an exponential (straight dashed lines).

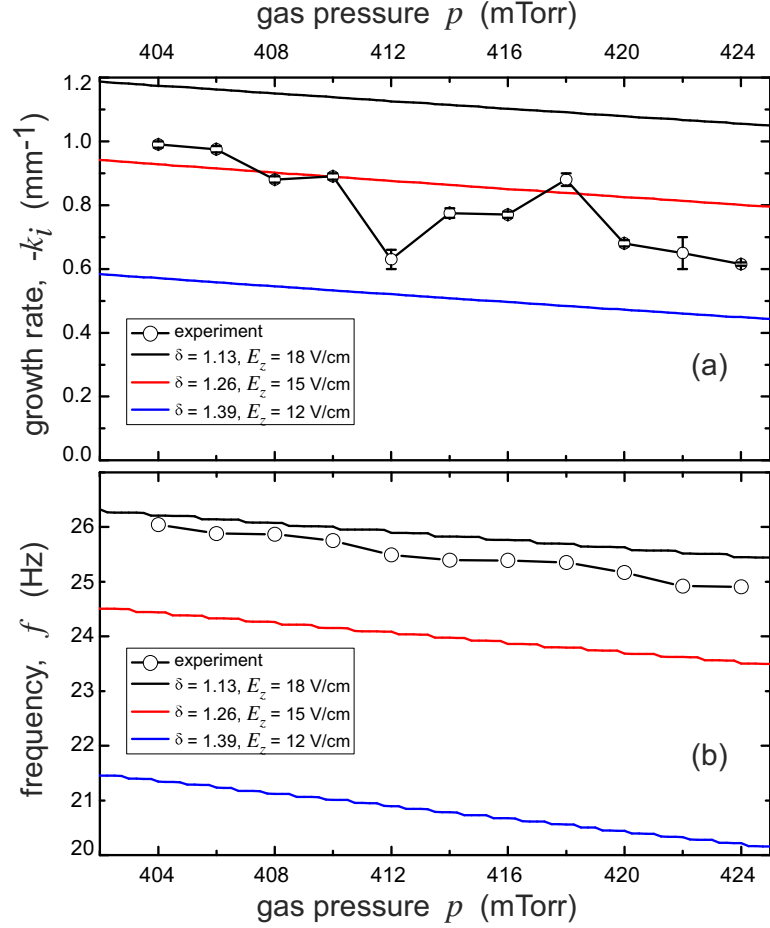


Figure 3.7: Variation with gas pressure p of (a) spatial growth rate k_i and (b) frequency f . The errors in the experimental k_i measurements shown here reflect variations due to the arbitrary choice of the range of z used in fitting the amplitude profile. Solid curves for the theory assume experimental parameters listed in Table A.1 (Appendix).

Saturation of the wave's growth in the lower region is an indicator of nonlinearity. (I report findings of a separate experiment studying DDW nonlinearities in Ch. 4 of this thesis.)

3.6 Fluid Model for Linear Waves

The dust-density wave dispersion relation in the case of strong Coulomb coupling is more difficult to derive than for weak coupling. There have been several

previous theoretical derivations, as reviewed by Piel and Melzer [64]. Generally, it is required to model the dusty plasma's microscopic structure, which creates local Coulomb potential wells between dust particles. Several approaches have been adopted to model how the collective wave motion is influenced by the strong-coupling effects associated with these local potentials. Rosenberg and Kalman [65] used the quasi-localized charge approximation, which is suited for disordered structures like liquids, to derive a dispersion relation. Kaw and Sen [66] used the generalized hydrodynamic description to include strong coupling effects amongst the dust particles in analyzing their elastic and viscous response to wave motion. Murillo used dynamical local field corrections to account for strong coupling effects [67]. In the dispersion relation that is derived next, I will use a simplified model for the dust cloud's microscopic structure.

At small amplitudes, dust-density waves are commonly described using a linear wave theory with three fluid components (electrons, ions, and dust) [43, 54]. Here, a similar model is developed that additionally includes an approximation of strong-coupling amongst the dust particles. So that the model is relevant to the experimental observations, it includes flowing ions and gas drag, which can excite and damp waves, respectively.

Assuming planar waves propagating in an infinite uniform plasma, the electrostatic dispersion relation is

$$\epsilon(k, \omega) \equiv 1 + \chi_e + \chi_i + \chi_d = 0 \quad (3.2)$$

where χ_e , χ_i , and χ_d are the susceptibilities for electrons, ions, and dust, respectively. Equation (3.2) is simply the Fourier transform of Poisson's equation [$\chi_j = -\tilde{n}_j Q_j / (\epsilon_o k^2 \tilde{\Phi})$], where $\tilde{\Phi}$ is the wave's electrostatic potential fluctuation and $\tilde{n}_j Q_j$ is the fluctuation in charge density for $j = (e, i, d)$. It is assumed that the wave number k is real, but the frequency ω is allowed to be complex. For each fluid

component, there is also a continuity equation and a momentum equation [43, 54], which I will not show here. For simplicity, the continuity equation is assumed to be sourceless (no local ionization or recombination), even though experiments suggest that ionization could be relevant in dust-density waves [55].

The electron and ion susceptibilities are derived in the usual way for weakly-coupled plasmas, from the linearized continuity and momentum equations. Because dust-density waves have a very low frequency, the wave frequency ω can be ignored in both χ_e and χ_i . An ideal-gas equation of state is assumed for the weakly coupled electrons and ions, so that their fluid pressures are $P_{e(i)} = n_{e(i)}k_B T_{e(i)}$, where $n_{e(i)}$ and $T_{e(i)}$ are the number density and temperature of electrons or ions. For the electron susceptibility χ_e , I assume the electrons have only random thermal motion with no bulk flow, so that

$$\chi_e = (k\lambda_{D_e})^{-2} \quad (3.3)$$

where k is the wave number and $\lambda_{D_e} = (\epsilon_0 k_B T_e / n_e e^2)^{1/2}$ is the electron Debye length. For the ion susceptibility χ_i , it is important (because it represents the source of instability) to include the flow of ions with velocity U_0 parallel to the wave vector. I also include a drag force on ions due to collisions with neutrals, at a collision rate ν_{in} , so that

$$\chi_i = \frac{\omega_{pi}^2}{(v_{T_i}^2 - U_o^2)k^2 + i\nu_{in}U_o k}. \quad (3.4)$$

This expression has both real and imaginary parts. It will be significant later, when discussing instability, that the imaginary part of χ_i is due to the ion flow U_o . Here, $\omega_{pi} = (n_i e^2 / \epsilon_0 m_i)^{1/2}$ is the ion plasma frequency and $v_{T_i} = (k_B T_i / m_i)^{1/2}$ is the ion thermal velocity.

The dust susceptibility χ_d is modeled differently than the electrons and ions for two reasons. First, since the massive dust particles provide the wave's inertia, the expression for χ_d must include the wave frequency ω . Second, the dust particles

are strongly coupled, unlike the electrons and ions, which are weakly coupled.

In this fluid model, the effects of strong coupling appear only in the dust pressure gradient term, $-\vec{\nabla}P_d$, of the dust momentum equation. The dust pressure gradient term is different than for the weakly coupled case, for example the ions in the plasma, where an ideal gas is assumed due to the rarity of ion-ion collisions. For the strongly-coupled dust, the dust fluid pressure P_d arises instead from Coulomb collisions of nearby charged dust particles.

To use the fluid model, one must find an appropriate expression for $-\vec{\nabla}P_d$. It is no trivial matter to model P_d for strongly-coupled plasmas, because the equation of state is more complicated than the simple ideal-gas equation that is used for weakly-coupled plasmas. In general, the equation of state for a strongly-coupled plasma could depend on its exact microscopic structure, for example a body-centered-cubic vs. a face-centered-cubic lattice for a solid, or something more disordered for a liquid. Rather than attempt to derive a model for the structure specific to this experiment, here I chose an approximate method.

I exploit the previous calculations of the longitudinal sound speed C_l in strongly-coupled dusty plasmas [68, 69]. One could, in principle, use a sound speed derived for any particular microscopic structure. Here, for simplicity, I use an expression [69] for C_l intended for the long-wavelength limit of a one-dimensional chain of particles interacting with a Yukawa potential, and assume a screening parameter $\kappa = 1$. The required physics in the equation of state is, for these purposes, provided by the sound speed. I make use of $C_l^2 = \partial P_d / \partial(m_d n_d)$, which assumes the dusty plasma is isentropic. The error introduced by this assumption is no larger than other uncertainties that will enter into my approximations below. Thus, I account for strong coupling amongst dust particles by using $-\vec{\nabla}P_d = -m_d C_l^2 \vec{\nabla}n_d$ in the dust momentum equation.

Accounting for dust inertia, strong coupling, and gas damping, it is found that

$$\chi_d = \frac{\omega_{pd}^2}{C_l^2 k^2 - \omega(\omega + i\nu_{dn})}. \quad (3.5)$$

Here, ω_{pd} is the dust plasma frequency. The neutral gas damping rate ν_{dn} entered the derivation of Eq. (3.5) in the dust equation of motion.

The dispersion relation can be algebraically solved for the complex frequency $\omega = \omega_r + i\omega_i$. Noting that χ_e and χ_i are independent of ω , one finds by substituting Eq. (3.5) into Eq. (3.2)

$$\omega(k) = -i\frac{\nu_{dn}}{2} + \sqrt{\frac{\omega_{pd}^2}{1 + \chi_e + \chi_i} + C_l^2 k^2 - \frac{\nu_{dn}^2}{4}}. \quad (3.6)$$

Strong-coupling effects appear in Eq. (3.6) in the term $C_l^2 k^2$.

I now assess the dispersion relation in Eq. (3.6) to determine the conditions for an instability. The DDW is unstable if $\omega_i > 0$, stable if $\omega_i < 0$, and critically stable if $\omega_i = 0$. One sees that an instability (and thus a self-excited DDW) is possible in this model by examining the two terms on the right-hand side of Eq. (3.6). The first term, arising from gas damping, is a purely negative imaginary number. However, the square-root term, arising from all the charged constituents, has both real and imaginary parts. The imaginary part of the square-root term, which comes from the $i\nu_{in}U_o k$ term in Eq. (3.4), is positive when the direction of wave propagation is aligned with the ion flow. Thus, gas damping tends to stabilize the wave, while ion flow tends to promote an instability that drives a DDW propagating parallel to the ion flow. Since ν_{dn} is proportional to gas pressure p , it is clear that this theoretical model can predict a critical gas pressure where $\omega_i = 0$. The accuracy of this prediction is limited by the approximations of the dust equation of state, among other things.

One would expect that a self-excited wave will be dominated by the most unstable k -mode. In other words, the k -mode with the highest growth rate ω_i is

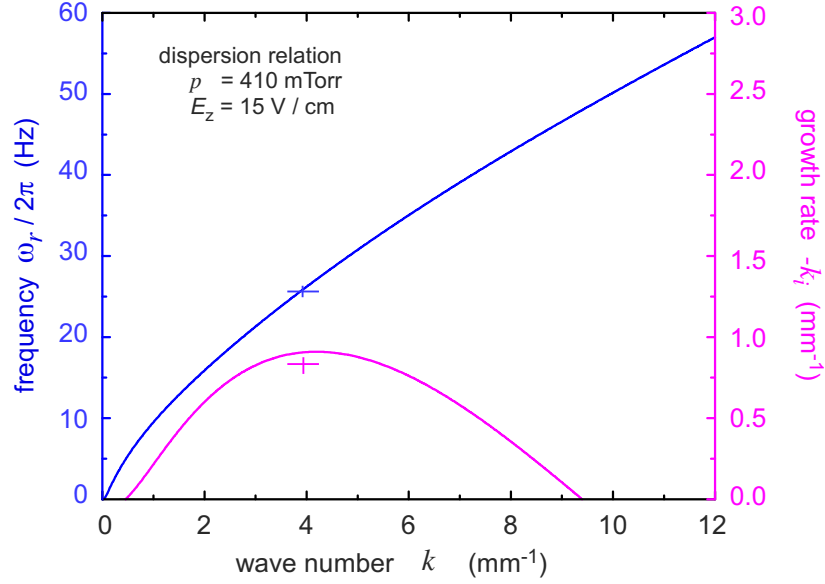


Figure 3.8: Theoretical dispersion relation (solid curves) for a gas pressure of 410 mTorr, calculated from Eq. 3.6. The real frequency is plotted in blue and the spatial growth rate in magenta. The most unstable k -mode predicted by the theory is close to the experimentally measured frequency and growth rate, which are shown as crosses. The model’s input parameters are listed in Table A.1.

the mode that should be observed. Thus, for the theoretically predicted mode, I select the k that maximizes the imaginary part of Eq. (3.6). Using the experimental parameters listed in Table A.1, the model’s most unstable k -mode is in agreement with the wave numbers observed in this experiment ($\sim 4 \text{ mm}^{-1}$). As an example, I have used Eq. 3.6 to calculate the dispersion relation for a gas pressure of 410 mTorr in Fig. 3.8. The k -mode for the maximum theoretical growth rate is near the experimentally observed wave number.

In solving the dispersion relation, a real k and a complex ω was assumed. However, in an experimental measurement of a spatial growth rate k_i , one presumes the point of view that k is the complex number and ω is real. In order to test the model against the experimental measurements (real ω and a complex k), I use the approximate expression [59] $\omega_i \approx -k_i v_g$. Here, $v_g = \partial\omega_r / \partial k_r$ is the DDW group

velocity, which can be calculated from Eq. (3.6). This relation is used to calculate $-k_i$ in Fig. 3.8

3.7 Experiment vs Linear Wave Theory

I will now examine whether the linear wave theory predicts my experimental results: a trend that growth rate diminishes with increasing gas pressure, and a critical gas pressure for the instability. I will make rough quantitative estimates of the growth rate predicted by the model, and compare to the experiment.

The theoretical and experimental growth rates are compared in Fig. 3.7(a) as a function of gas pressure. I note that they exhibit the same trend: the growth rate diminishes with gas pressure. Exact numerical agreement is not expected for several reasons: the theory is purely linear, some experimental parameters required in the theory are not precisely known (see Appendix A.1), and the theory is for a spatially unbounded plasma. The finite 5-mm height of the experimental dust cloud prevents detecting any $k_i < 0.2 \text{ mm}^{-1}$. Theoretical results are shown for several representative estimates of experimental parameters.

Earlier, it was found in the experiment that the frequency f diminishes with gas pressure (Fig. 3.5). This trend is also exhibited by the theory, as shown in Fig. 3.7(b).

The theoretical model also predicts a critical gas pressure, just as I observe in the experiment. Extrapolating the three theoretical curves in Fig. 3.7(a) to higher gas pressures, the curves all have zeroes, which correspond to the theoretical critical gas pressure. For the curves in Fig. 3.7(a), the theoretical critical pressure is in the range 530 to 710 mTorr, which is higher than the observed critical gas pressure of 424 mTorr.

3.8 Summary

In a laboratory dusty plasma experiment, I observe the spatial growth of self-excited dust density waves. By observing the dust cloud at various gas pressures, I find that a DDW self-excites at a critical gas pressure, due to an ion flow instability that just overcomes neutral gas damping. At pressures near and just below this critical gas pressure, the wave amplitude grows as it propagates through the dust cloud.

As the main result of this chapter, I measured the spatial growth rate $-k_i$ of dust-density waves near the instability threshold. To do this, I developed a method of measuring amplitude that is phase sensitive. This method yields a spatial profile of the wave's amplitude and phase. Fitting the amplitude profile to an exponential yields the growth rate $-k_i$. The results revealed a trend that the growth rate increases as gas pressure decreases. The frequency exhibits the same trend.

Additionally, I compare the experimental results with a linear wave theory that includes the effects of strong coupling. The theory shows the same trends that growth rate and frequency decrease as gas pressure increases. As expected, the theory predicts a critical gas pressure for a self-excited DDW. The theory's assumption of small-amplitude waves is most likely to be valid near the instability threshold, which is where the experiment was performed.

CHAPTER 4

DEVELOPMENT OF NONLINEARITY IN A GROWING SELF-EXCITED DUST-DENSITY WAVE

4.1 Introduction

The work presented in this chapter is a continuation of the study of dust-density waves, which were introduced in Ch. 3 of this thesis. Dust-acoustic waves, also termed dust-density waves, are low-frequency compressional waves that propagate in dusty plasma [43]. The dust-density wave (DDW) is analogous to the ion-acoustic wave. In the DDW, the heavy dust particles provide the wave's inertia, while charge separation due to the dust and the background electrons and ions provides a restoring electric field. The electric forces can be large because the dust particles have a large negative charge. Because the dust particles are so heavy, the DDW frequency is very low. Thus, the wave can be observed in the laboratory using video imaging [41].

As shown, for example, in Ch. 3, the DDW often self-excites in dusty plasma due to an instability driven by ion flow [56, 58]. This has been observed in several experiments, both in the laboratory [42, 73, 44, 49, 74, 59, 50, 75, 76] and under microgravity conditions [54, 77]. In laboratory experiments, such as the one reported in this chapter, dust particles are often levitated in the plasma sheath, where ion flows can be strong enough to couple their energy to dust particles, driving the wave [56].

The DDW can be driven to large amplitudes, where a variety of nonlinear effects have been observed. Shocks have been shown to develop as a DDW steepens

[78, 47], and the confluence of shocks has been observed [48]. Nonlinear wave-particle interaction [50, 51, 79] and wave breaking [52] have been observed in experiments that allow identification of individual particles. Turbulence [80], spatial frequency clustering [62], and wave harmonics [51, 52] have also been observed. These experiments were mostly performed under conditions where dissipation could not stop the wave from growing to large amplitudes.

The DDW is damped by collisions between dust particles and neutral gas, which is always present in dusty plasma experiments. At high gas pressures, the dust-neutral collision rate ν_{dn} is so large that the wave is not observed, while at low gas pressures, gas damping is less effective and the DDW can grow to large amplitudes [58]. At a *critical* gas pressure, the instability and gas damping effects balance, which determines a threshold for wave excitation [74, 50, 58]. At gas pressures of about 1 Torr (1 atm = 760 Torr), the time scale for gas damping of dust motion ν_{dn}^{-1} is comparable to a typical wave period. For a spherical dust particle of radius r_d and mass density ρ_d , the dust-neutral collision rate is $\nu_{dn} = \sqrt{8k_B T_g m_g} \delta n_g / \rho_d r_d$, where m_g is the mass of a gas atom, T_g and n_g are the gas temperature and number density, and δ is a constant of order unity that must be measured [70]. Because ν_{dn} is proportional to n_g , it is also proportional to gas pressure. In the experiment reported in this chapter, I reduce the effect of gas damping by decreasing the gas pressure. In addition to neutral gas damping, other damping mechanisms have been proposed, such as wave damping due to a fluctuating dust particle charge [81, 82, 83].

Here, I report observations of the development of nonlinearity in a coherent self-excited DDW. As gas pressure p is gradually reduced (i.e., gas damping), at first a small amplitude wave is observed. As p reduces further, the wave amplitude increases and the nonlinearities develop. Nonlinearities are identified by detecting

harmonics. I measure the harmonic amplitudes, wave numbers and growth rates using the phase-sensitive detection developed in Ch. 3. As gas pressure p reduces I find three conditions: at higher p the harmonics are indistinguishable from noise; at intermediate p the harmonic energies emerge from the noise and increase exponentially as p decreases; and finally at lower p the harmonic amplitudes saturate. I find that the values of the wave numbers k_r and growth rates $-k_i$ for the second harmonic (frequency $2f$) are double those for the fundamental (frequency f). Similarly, k_r and $-k_i$ for the third harmonic ($3f$) are triple those for the fundamental.

4.2 Experimental Design

The experiment is designed to observe the development of nonlinearity in a naturally occurring dust-density wave. To do so, I begin the experiment under conditions where the dusty plasma exhibits little or no wave activity. About 10^5 dust particles (4.8- μm diameter) are introduced into an argon plasma. The dust particles become negatively charged and are levitated in the plasma sheath's vertical electric field, filling a volume in the plasma near the bottom of the glass box (the same box used in the experiment in Ch. 3). The box rests on the same rf powered electrode (85 V_{pp}) as in Ch. 3, so that the dust particles are confined in a similar dust cloud. The dust cloud has many horizontal layers, with overall dimensions of 22-mm width and 6-mm height.

The DDW amplitudes, and therefore the expected nonlinear effects, vary sensitively with gas pressure p , which leads me to design an experiment where p is varied over many finely-spaced values. Therefore, I choose to sample data as I vary the gas pressure slowly and gradually (see Fig. 4.1), rather than record data at discrete pressure levels, as I did in the experiment reported in Ch. 3. (This is the most substantial difference between the experimental procedures used here and in Ch. 3.) As p is slowly decreased, the dust cloud is viewed from the side using a high-speed

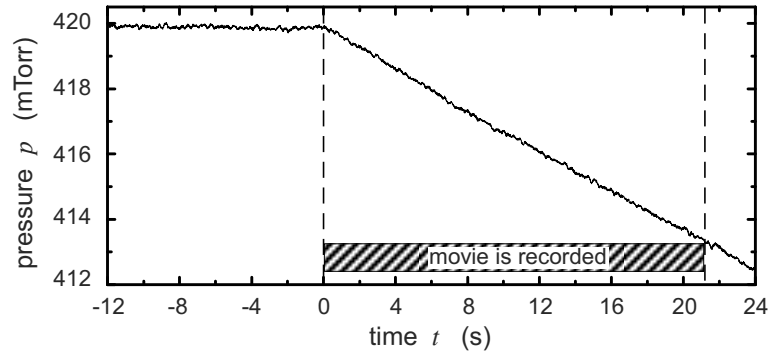


Figure 4.1: Time series measurement of gas pressure p , which is the experimental parameter used to control the instability and growth of the dust-density wave. The pressure is constant until time $t = 0$, when p begins to decrease at a linear rate. At the same time, a movie begins recording, which provides the principal data for the experiment.

camera that records a 21 s movie at 500 frames per second. The movie images provide the principal data for the experiment. The image intensity is proportional to dust number density, as explained in Sec 3.2.

The experiment begins with a dust cloud at $p = 420$ mTorr, which is just below the critical gas pressure so that wave activity is barely detectable. At this pressure, the gas damping rate is $\nu_{dn} = 135$ s⁻¹. A side view image of the dust cloud under these conditions is shown in Fig. 4.2(a). In this stable dust cloud, the dust particles tend to line up in vertical chains. This vertical alignment is due to the downward ion flow, which is the same flow that can excite the DDW.

I use a pressure control system to continuously decrease the gas pressure, Fig. 4.1. The control system consists of a capacitance manometer pressure sensor, a butterfly exhaust valve to regulate the pumping speed, and a feedback controller that adjusts the valve in order to match the pressure measurement to a desired set point. In order to ramp the pressure linearly with time, I apply a corresponding voltage waveform to the controller's set point. Only the exhaust valve is adjusted in this control system; the inlet gas flow remains constant at 5 sccm (standard cubic

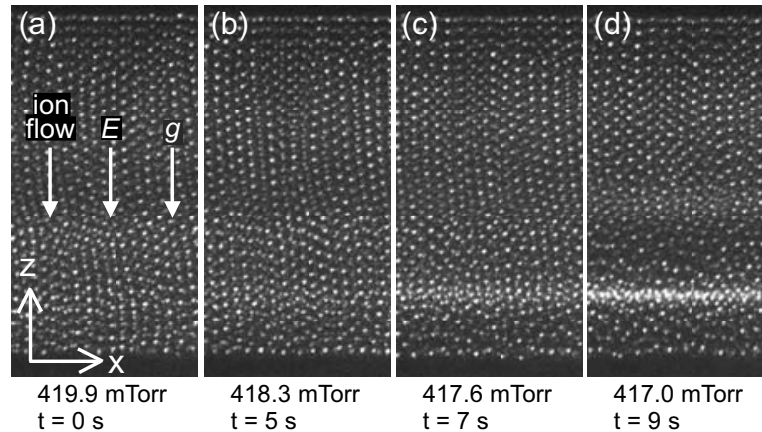


Figure 4.2: Side-view images of the dust cloud’s central region. Bright spots are individual dust particles. Depending on the gas pressure, the ion-flow instability can cause planar compressional waves to grow in amplitude as they propagate downward in the $-\hat{z}$ direction. (a) At the highest pressure, gas damping causes the wave to be barely detectable. (b)-(d) At lower gas pressures, gas damping is less effective and the wave grows to higher amplitudes, as indicated by the bright high-density wave fronts near the bottom of the dust cloud. Each panel shows the same $2.95 \text{ mm} \times 5.90 \text{ mm}$ spatial region.

centimeters per minute).

In choosing the pressure ramp rate, it is required to observe multiple wave transits under nearly steady conditions. (A wave transit is the time required for the DDW to propagate through the dust cloud’s vertical extent, 0.15 s.) In simple terms, a slower ramp rate is better. The most restrictive conditions for meeting this requirement are found in an intermediate pressure range, where wave amplitude is most sensitive to pressure. I found that in the intermediate pressure range, harmonic energies increased by a factor e over a pressure change of 0.24 mTorr. I chose a ramp rate to be slow enough that there are multiple wave transits during the time interval that the pressure changes by 0.24 mTorr. The ramp rate used was -0.31 mTorr/s , corresponding to a 0.01% variation of pressure p and damping rate ν_{dn} during one wave transit. (In separate tests using faster ramp rates, conditions were not sufficiently steady during a wave transit.) The movie’s entire duration of

21 s corresponds to 140 wave transits.

4.3 Wave Amplitude Observations

The results of this experiment are all based on the recorded movie, which reveals a coherent self-excited dust-density wave. The wave has a nearly planar geometry. The wave propagates downward through the dust cloud in the $-\hat{z}$ direction, parallel to the ion flow, with a speed of 40 mm/s and a frequency of 25.0 Hz.

Nonlinear effects are expected where wave amplitudes are highest, which occurs in this experiment near the bottom of the dust cloud and at lower gas pressures. Near the bottom of the cloud, the amplitude is large because the wave grows as it propagates downward. This spatial growth is due to the ion-flow instability, which drives the wave. The spatial growth is prominently indicated by the increasing amplitude of the wave fronts near the bottom of the dust cloud in Fig. 4.2(d), as compared to the top. Lower gas pressures also lead to higher amplitudes because gas friction is reduced. Gas friction is an energy loss mechanism that competes with the instability [58]. The variation of wave amplitude with gas pressure can be seen by comparing the four panels of Fig. 4.2, and by noting that for a given height z , the wave amplitude increases as the pressure is lowered.

4.4 Analysis Methods

The three main methods used to analyze the recorded movie are calculations of space-time data, power spectra, and the phase-sensitive amplitude detection. These are all based on analyzing video images, where the brightness of the image is proportional to dust number density. Details of these three methods are presented next.

The first method used is a calculation of space-time data, which represent image intensity as functions of both vertical position z and time t . The calculation

begins with the individual video images, cropped to the spatial region shown in the panels of Fig. 4.2 (5.90 mm vertical and 2.95 mm horizontal). Exploiting the planar nature of the waves in this region, I average over the ignorable coordinate x , yielding data corresponding to dust number vs vertical position z (just as was done in Ch. 3). All the required information needed to analyze a compressional planar wave is incorporated into the space-time data: a quantity representing dust number density as a function of both position z and time t . With the exception of the images' cropped region, all details of space-time data calculation are the same as those described in Sec. 3.4.1. Here, I do not present the space-time data in visual form (as a diagram), but still use it in all subsequent analysis.

The second method used is an identification of the frequencies present in the wave using power spectra, computed as functions of vertical position z . For a given height z , a power spectrum is computed using an FFT of a 1024-frame time series (~ 2 s) from the space-time data. This is repeated for thirty vertical positions z . Assembling the power spectra for each value of z yields a plot of wave energy as a function of both frequency and height. These spatially-resolved plots of the power spectrum will reveal a fundamental frequency as well as the presence of harmonics. The fundamental frequency, as measured by this method, is required for the phase-sensitive detection.

The third method used is the phase-sensitive amplitude detection, which yields precise measures of the wave's phase ϕ and amplitude A as functions of the vertical position z . This is the same analysis method used to measure the growth rates in Ch. 3 of this thesis. However, here, the wave is analyzed for the harmonic modes, in addition to the fundamental. As stated in Sec. 3.4.3, this method requires that the frequency does not vary with position z , and that it varies slowly or not at all with time. These requirements are satisfied in this experiment.

My chief results of this chapter, in Sec. 4.5, are based on the phase-sensitive detection, yielding spatially-resolved measurements of amplitude A and phase ϕ . Because the waves are planar, I can calculate vertical spatial profiles $A(z)$ and $\phi(z)$. I use the profiles to compute wave number k_r , and growth rate $-k_i$, for the middle and upper portions of the dust cloud. In these regions, the wave is only weakly nonlinear and it has not yet propagated far enough for its growth to saturate. Essentially, I assume planar waves with a dust number density $\propto e^{ikz - i2\pi ft}$, where the real part of $k = k_r + ik_i$ is the wave number and the imaginary part is the spatial growth rate. (This assumption applies not only to the fundamental but also the harmonics, except in the lower part of the dust cloud where the wave's amplitude saturates and no longer grows as $e^{-k_i z}$). In Sec. 4.5, I report wave numbers (k_{r1}, k_{r2}, k_{r3}) , and spatial growth rates $(-k_{i1}, -k_{i2}, -k_{i3})$, corresponding to the fundamental f and its first two harmonics $2f$ and $3f$.

4.5 Results

4.5.1 Fundamental frequency

The fundamental frequency of the wave is $f = 25.0$ Hz. This measurement is based on the power spectrum, Fig. 4.3. I found that f did not vary significantly with vertical position z or gas pressure p . (There would have been more noticeable gas pressure dependence if the pressure range studied were larger. However, nonlinearities developed over a very small pressure range.)

4.5.2 Nonlinear development with diminishing pressure

I present several results to study the development of a nonlinear wave as gas pressure p decreases. I begin by observing the presence of harmonics in the power spectrum. I then use phase-sensitive detection to quantify how the harmonics

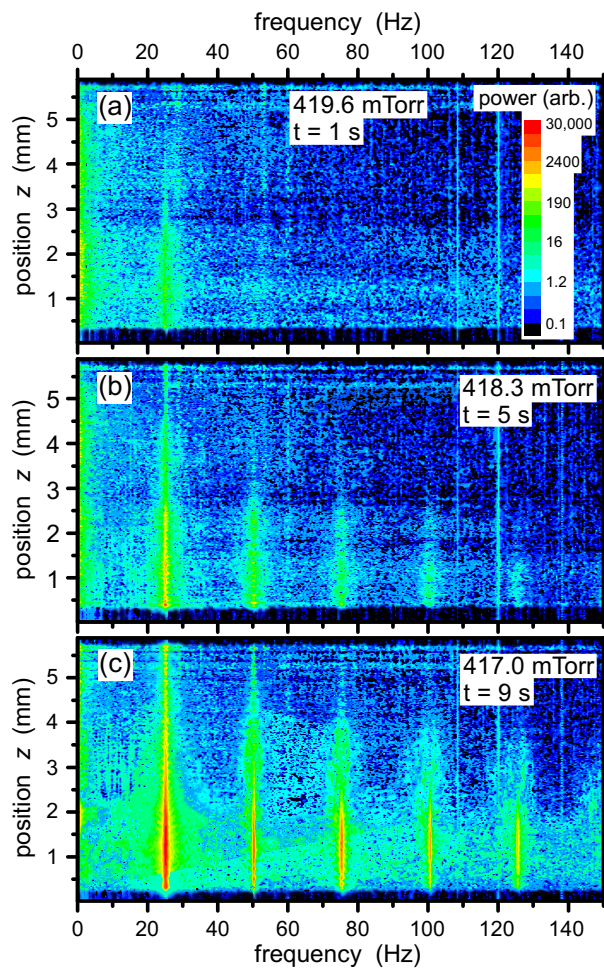


Figure 4.3: Power spectra plotted vs. vertical position z for three gas pressures. The fundamental frequency is $f = 25.0$ Hz. (a) At high gas pressures, I can detect only the fundamental and only at lower values of z . (b)-(c) At lower pressures, harmonics become stronger. At 417 mTorr, I can detect all nine harmonics that are below the Nyquist frequency of 250 Hz (half the camera's frame rate); only the first four harmonics are shown. These spectra are calculated from the space-time data. Each panel corresponds to a sequence of 1024 frames, i.e. 2 s of data, centered at the times indicated.

emerge, grow, and then level off as the gas pressure is diminished.

The presence of harmonics is a signature of nonlinearity, and is revealed in the power spectra (Fig. 4.3). The energy in the harmonics exhibits the same general trends as the energy of the fundamental: all become stronger at lower gas pressures and near the bottom of the dust cloud, i.e., at small z . At higher pressures, the wave amplitude is very small so that only the fundamental is detectable, especially near the bottom of the dust cloud, as in Fig. 4.3(a).

The growth and saturation of the fundamental and harmonics is revealed by the phase-sensitive detection. For a position near the bottom of the dust cloud, as in Fig. 4.4(a), the fundamental amplitude A_1 increases exponentially with decreasing pressure, after emerging from noise. This exponential increase is abrupt, with the amplitude doubling several times as the pressure is reduced only a fraction of one percent. As p decreases further, the exponential variation ceases and the amplitude levels off. The harmonics exhibit the same trends as pressure decreases: emerging from noise, then increasing exponentially, and finally leveling off at lower pressures. However, compared to the fundamental, the harmonics emerge from noise at slightly lower pressures and level off at lower amplitudes.

As a simple indicator of nonlinearity, I use the total harmonic distortion (THD), which is the ratio of the total power in the harmonics to the power in the fundamental. In Fig. 4.4(b), I calculate the THD as $(A_2^2 + A_3^2)/A_1^2$, using the amplitudes from Fig. 4.4(a). Nonlinearities, as measured by THD, emerge from the noise level at a pressure of about $p = 418.2$ mTorr. The nonlinearity then increases exponentially as p is reduced, $\propto e^{-p/p_o}$. Fitting the data in Fig. 4(b) I find a small value for the fit constant of $p_o = 0.24$ mTorr. The exponential increase of nonlinearity does not continue indefinitely as p decreases. In fact, it occurs only over a limited range of pressures. The THD saturates at a level of about 45%. In

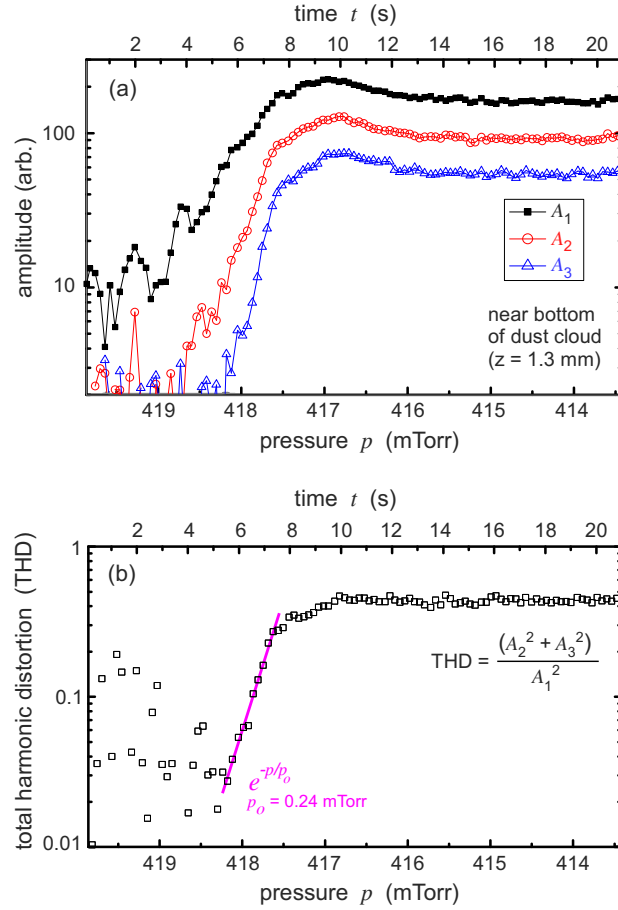


Figure 4.4: Development of nonlinearity. (a) Amplitudes of the fundamental A_1 , the second harmonic A_2 and the third harmonic A_3 . As pressure p decreases, the amplitudes increase exponentially from noise levels and then saturate. The amplitudes are calculated for a position near the bottom of the dust cloud. (b) Total harmonic distortion (THD), an indicator of nonlinearity, calculated from the amplitudes in (a). After emerging from noise, the THD increases exponentially as p decreases, with a pressure constant p_o , and then saturates. At saturation, $\text{THD} = 45\%$, i.e., the harmonic energy is almost half the fundamental energy. Noise at higher pressures is due to small wave amplitudes. In both panels, the gas pressure scale is reversed (bottom axis). Results here and in Fig. 4.6 are computed from the space-time data using phase-sensitive detection.

other words, the nonlinearity increases to a maximum level where energy in the harmonics is almost half the energy in the fundamental. This 45% THD was measured for a position $z = 1.3$ mm near the bottom of the dust cloud. At higher positions, the nonlinearities are weaker, with a THD of 40% at $z = 2.0$ mm and 10% at $z = 3.0$ mm.

4.5.3 Wave numbers and growth rates of harmonics

Each measurement of wave number and growth rate is based on a corresponding vertical profile of the amplitude (A_1 , A_2 , or A_3) or the phase (ϕ_1 , ϕ_2 , or ϕ_3). As an example, the vertical profiles of all of these quantities are presented in Fig. 4.5 for time $t = 10.0$ s, corresponding to the gas pressure $p = 416.8$ mTorr. The phase data show that higher harmonics have higher wave numbers, and they are not detected until the wave has partially propagated through the dust cloud, as shown in Fig. 4.5(a)-(c). The amplitude data show that the harmonics grow at faster rates than the fundamental, but never overcome the fundamental [Fig. 4.5(d)]. All amplitudes saturate near the bottom of the dust cloud, at lower values of z .

Results for measurements of the wave numbers k_r and the growth rates $-k_i$ are presented in Fig. 4.6. After the pressure is decreased sufficiently for waves to be measured using phase-sensitive detection, the wave number k_r does not vary noticeably with pressure. This lack of variation is true not only for the fundamental, but also the harmonics, as shown in Fig. 4.6(a). The growth rates $-k_i$ have a slight trend to increase as p decreases, as shown in Fig. 4.6(b). In a separate experiment reported in Ch. 3, I noted this trend for the fundamental $-k_{i1}$; here, I note the same trend for the harmonics $-k_{i2}$ and $-k_{i3}$. The noise at high pressures in Fig. 4.6(a) and Fig. 4.6(b) is due to waves that are too weak for precise measurements using phase-sensitive detection.

Measurements of wave number allow us to gain an understanding of the wave's

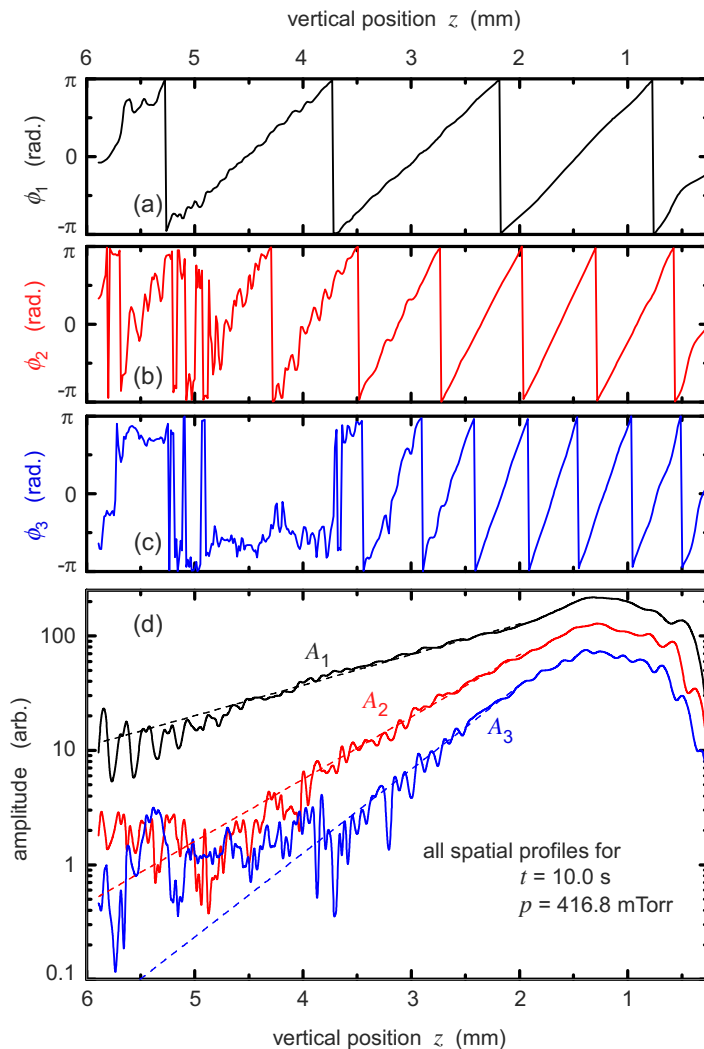


Figure 4.5: Vertical profiles of (a)-(c) the wave's phase ϕ and (d) the wave's amplitude A , corresponding to gas pressure $p = 416.8$ mTorr. Results are shown for the fundamental wave mode (ϕ_1, A_1) and its second and third harmonics, (ϕ_2, A_2) and (ϕ_3, A_3). Profiles like these are calculated from space-time data using phase-sensitive detection. These profiles are then used to measure the wave numbers k_r and growth rates $-k_i$.

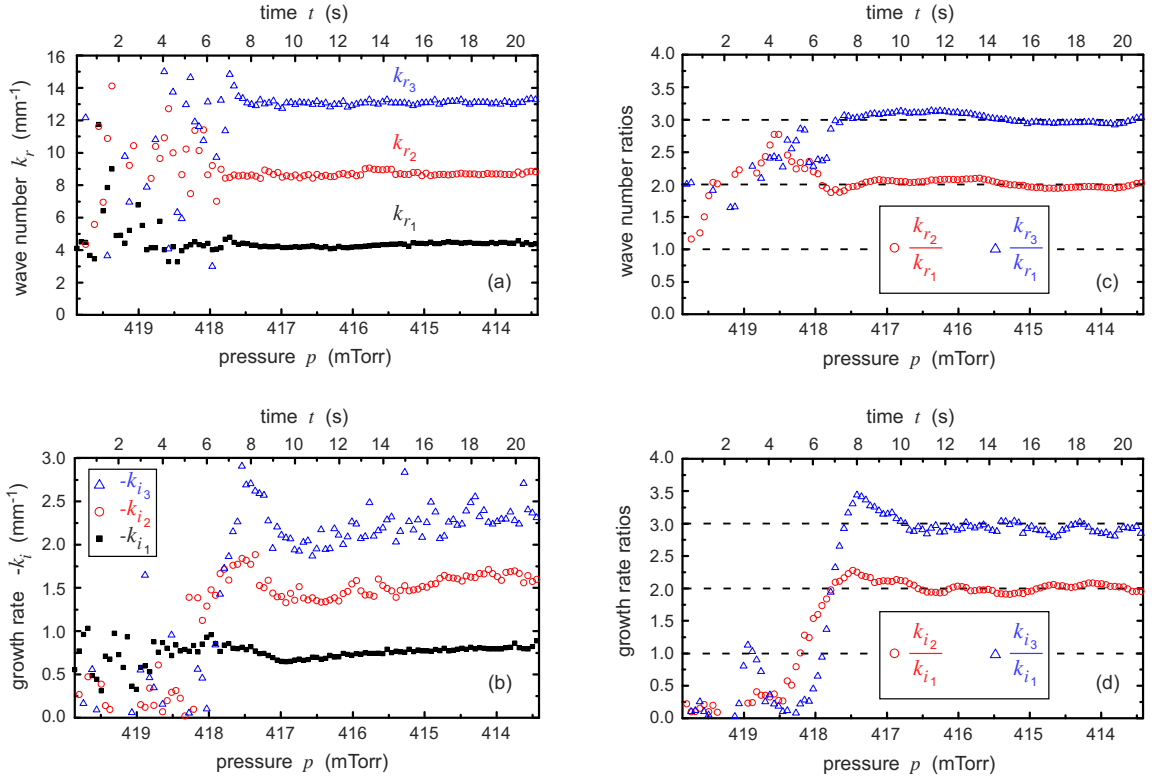


Figure 4.6: Measurements of (a) wave numbers k_r and (b) growth rates $-k_i$ as a function of gas pressure p . In panel (a), the real wave numbers for the fundamental mode k_{r1} , second harmonic k_{r2} , and third harmonic k_{r3} do not vary with p . In panel (b), the growth rates of the same modes $-k_{i1}$, $-k_{i2}$, $-k_{i3}$ increase slightly as p decreases. (c) Wave number ratios k_{r2}/k_{r1} and k_{r3}/k_{r1} are close to two and three, respectively, when nonlinearity develops at lower pressures. (d) Growth rate ratios k_{i2}/k_{i1} and k_{i3}/k_{i1} are also two and three. In panels (a) and (b), scatter at higher pressures is due to small wave amplitudes, which lead to noise in measurements of k_r and k_i . In panels (c) and (d), adjacent averaging is used to smooth data before calculating the ratios. Pressure and time scales are the same as in Fig. 4.4.

nonlinearities. Consider two undamped waves, l and m , that interact to generate a third wave n . The frequencies are expected to add as

$$f_n = f_l + f_m. \quad (4.1)$$

If the waves propagate in the same direction, and the waves are dispersionless, $f \propto k$, one would expect that wave numbers will add as

$$k_n = k_l + k_m \quad (4.2)$$

for both the real and imaginary parts of the wave number. (A dispersionless wave has a phase speed that does not vary with k_r .) The generation of a second harmonic $2f$, for example, corresponds to $f_l = f_m = f$, where f is the fundamental frequency. For the generation of a second harmonic one would expect the wave numbers to have a simple ratio $k_{r2}/k_{r1} = 2$, for example.

As a chief result, I find that the development of harmonics, as a result of nonlinearities, obeys Eq. (4.2). Using the data in Fig. 4.6(a), I compute ratios of the wave number k_r for the harmonic frequencies. The result, in Fig. 4.6(c), is a doubling and tripling of k_r : k_{r2}/k_{r1} is in the range 1.95 to 2.09, and k_{r3}/k_{r1} is in the range 2.92 to 3.12. Similarly, using the data in Fig. 4.6(b), and computing the ratios of growth rates k_i , I find in Fig. 4.6(d) a doubling and tripling of k_i : k_{i2}/k_{i1} is in the range 1.92 to 2.07, and k_{i3}/k_{i1} is in the range 2.82 to 3.04. The doubling and tripling of k_r and k_i for the harmonics indicates that the nonlinear wave in this experiment obeys Eq. (4.2). The frequency relation in Eq. (4.1) is also obeyed, as shown in Fig. 4.3.

The data analysis method used here is analogous to a method used previously to characterize harmonic content of beam-driven Langmuir waves [84, 85, 86, 87]. The waveform measured by a detecting probe was analyzed by a lock-in amplifier, which provides phase-sensitive detection similar to the one used in my analysis.

Malmberg and Wharton [84], Mizuno and Tanaka [85], and Mori [86] measured growth rates $-k_i$ of the fundamental and harmonics using interferometry. They found that $-k_i$ doubled for the second harmonic and tripled for the third harmonic. However, measurements of higher harmonics and measurements of k_r were not reported. In similar experiments, Apel [87] measured k_r and $-k_i$ for several harmonics and found that they were higher than for the fundamental, but did not claim they were multiples of the fundamental. The Langmuir waves in these experiments were self-excited as the result of a beam-plasma instability, which is analogous to the ion-flow instability that drives the (much lower frequency) DDW in my experiment.

4.6 Summary

In a dusty plasma experiment, I study nonlinearity in a naturally occurring dust-density wave, which grows as it propagates. The wave is driven by an ion-flow instability, and is damped by neutral gas drag. At a critical gas pressure, these competing effects balance and no wave is observed. I reduce the gas pressure (i.e., gas damping) as I image the dust cloud, allowing me to observe the instability overcome damping and drive the wave to larger amplitudes.

As the first main result of this chapter, I observe the development of nonlinearity in the dust-density wave. The nonlinearity is indicated by the presence of harmonics with large amplitudes. As pressure is reduced, a small amplitude wave with a fundamental frequency develops into a nonlinear wave with many harmonics and saturated amplitude.

As the second main result, I measured the wave numbers k_r and growth rates $-k_i$ of the fundamental, second, and third harmonic modes, using a phase-sensitive detection. Compared to the fundamental wave number and growth rate, the second and third harmonics are doubled and tripled, respectively. This would be expected if the dust-density wave was dispersionless and undamped. Although I do not know

of any similar measurements in a dusty plasma experiment, similar results have been found in experiments on Langmuir waves that are driven by a beam-plasma instability.

CHAPTER 5

SUMMARY

In this thesis, I report the findings of three separate dusty plasma experiments. In addition to the charged dust particles, neutral gas plays a large role in all three experiments. In each of these laboratory experiments, a dusty plasma is confined within the volume of a glass box, so that the vertical box walls can enhance the plasma's horizontal electric field. The enhanced field allows for confining a dusty plasma that fills a volume, instead of a single plane. The first experiment was designed to demonstrate thermal creep flow, which is a flow of gas that is driven by a gas temperature gradient along a solid surface. The second and third experiments were designed to study the growth of naturally occurring dust-density waves, and to study some of the wave's nonlinear properties.

In Ch. 2, dust particles suspended in a spherically-shaped dusty plasma (Yukawa ball) served as indicators of thermal creep gas flow. A high-power laser was used to locally heat two glass boundaries, setting up tangential gas temperature gradients. As a consequence of this heating, a stirring motion was observed in the Yukawa ball, which was attributed to a bulk gas flow driven by TCF at the heated surfaces. In Sec. 2.4, I presented logic to dismiss all alternative effects that might account for the stirring. This experimental test serves two purposes, for two different scientific communities. For the fluid mechanics community, it serves as a rare experimental verification of the existence of TCF. For the plasma physics community, it verifies the recently reported demonstration [17] that TCF can have a significant effect on dusty plasmas. The experiment here differs from the one used in Ref. [17] in several ways. My configuration is designed so that TCF results in a horizontal flow, to allow distinguishing it from convection. Also, TCF is driven by an optical heating method that is independent of the dusty plasma's confinement forces, so that the

effect of TCF can be turned on and off.

In Ch. 3, I observe the spatial growth of a naturally occurring dust-density wave (DDW). The wave propagates downward through a dust cloud that has many horizontal layers. By observing the dust cloud at various gas pressures, I find that the DDW self-excites at a critical gas pressure, due to an ion flow instability that barely overcomes neutral gas damping. At pressures near and just below this critical gas pressure, the wave amplitude grows as it propagates through the dust cloud. As the main result, I measured the wave's growth rate using a phase-sensitive amplitude detection method. The results revealed a trend that the growth rate increases as gas pressure decreases. To my knowledge, this is the first time a that a DDW growth rate has been measured near the instability threshold. A theoretical fluid model was developed to describe the wave, and it was compared with the experimental findings. The theory's assumption of small-amplitude waves is most likely to be valid near the instability threshold, which is where the experiment was performed.

In Ch. 4, I observe the development of nonlinearity in a dust-density wave. The nonlinearities, as indicated by harmonics, develop in response to the gradually decreasing gas pressure. The experimental conditions are similar to those in Ch. 3. However, the important difference is that instead of making separate observations at discrete gas pressures (Ch. 3), here I make observations as the gas pressure is decreased with time. In doing so, I observe a small-amplitude wave develop into a nonlinear wave with many harmonics and saturated amplitude. To my knowledge, this is the first time such an observation has been reported in a dusty plasma experiment. The analysis methods used are also similar to those in Ch. 3, relying mainly on phase-sensitive detection. The main difference is that in Ch. 4 I analyze not only the fundamental mode, but also its harmonics. I measured the wave amplitudes A , wave numbers k_r , and growth rates $-k_i$ for the fundamental mode and the second

and third harmonics. As pressure decreases, the harmonic amplitudes increase exponentially over a very small pressure range, and then saturate as pressure decreases further. Compared to the fundamental wave number and growth rate, the second and third harmonics are doubled and tripled, respectively.

APPENDIX A

ESTIMATES OF DDW EXPERIMENTAL PARAMETERS

Here we present estimates of some experimental parameters to test the linear wave theory, in Sec. 3.7. The two input parameters that have the largest effect on the theoretically-predicted growth rates are the vertical electric field E_z (since $E_z \propto U_o$, the ion-flow instability source) and the Epstein collision rate ν_{dn} (since it directly affects wave damping). Thus, in Table A.1, we provide an uncertainty range for estimates of E_z and ν_{dn} , [70] along with justification for their estimated values. Also in Table A.1, we list estimates of all other input parameters in the theoretical model. We have verified that our estimates of E_z , n_e , n_i , T_e , and T_i are reasonable by performing a fluid simulation of our experiment's entire discharge. [72]

Table A.1: Experimental Input Parameters for Linear Wave Model

PARAMETER	ESTIMATE		COMMENT
	Value	Expression	
<u>measured</u>			
n_e	$2 \times 10^8 \text{ cm}^{-3}$		Langmuir probe
T_e	6 - 8 eV		Langmuir probe
T_i	1/40 eV		room temperature
n_d	$1.2 \times 10^5 \text{ cm}^{-3}$		image analysis
cloud height	4.5 - 5.0 mm		image analysis
<u>known</u>			
$m_d g$	$8.6 \times 10^{-13} \text{ N}$		manufacturer
<u>assumed</u>			
κ	1		Arp <i>et al.</i> [10]
δ	1.26 ± 0.13		Liu <i>et al.</i> [70]
<u>computed</u>			
$\nu_{dn}[\text{s}^{-1}]$		$255 \delta p[\text{Torr}]$	Liu <i>et al.</i> [70]
$-E_z$	$15 \pm 3 \text{ V/cm}$		$T_e/(\text{cloud height})$
$\mu_+[\text{cm}^2/\text{V} \cdot \text{s}]$		$1052/p[\text{Torr}]$	Frost [71]
$U_o[\text{cm/s}]$		$1052 E_z[\text{V/cm}]/p[\text{Torr}]$	$\mu_+ E_z$
$\nu_{in}[\text{s}^{-1}]$		$2.34 \times 10^7 p[\text{Torr}]$	$e/(m_i \mu_+)$
Z_d	4000		$e Z_d E_z = m_d g$
C_l	23 mm/s		Wang <i>et al.</i> [69]
<u>simulated</u>			
n_i	$6 \times 10^8 \text{ cm}^{-3}$		fluid simulation [72]

REFERENCES

- [1] C.K. Goertz, *Rev. Geophys.* **27**, 271 (1989).
- [2] R.L. Merlino and J. Goree, *Phys. Today* **57**, Iss. 7, p. 32 (2004).
- [3] J.E. Wahlund *et al.*, *Planet. Space Sci.* **57**, 1795 (2009).
- [4] G.S. Selwyn, J. Singh, and R.S. Bennett, *J. Vac. Sci. Technol. A* **7**, 2758 (1989).
- [5] B.M. Jelenković and A. Gallagher, *J. Appl. Phys.* **82**, 1546 (1997).
- [6] P. Roca i Cabarrocas, Y. Djeridane, Th Nguyen-Tran, E.V. Johnson, A. Abramov and Q. Zhang, *Plasma Phys. Control. Fusion* **50**, 124037 (2008).
- [7] Y. Feng, J. Goree, and B. Liu, *Rev. Sci. Instrum.* **78**, 053704 (2007).
- [8] O. Havnes, C.K. Goertz, G.E. Morfill, E. Grün, and W. Ip, *J. Geophys. Res.* **92**, 2281 (1987).
- [9] H. Rothermel *et al.*, *Phys. Rev. Lett.* **89**, 175001 (2002).
- [10] O. Arp *et al.*, *Phys. Plasmas* **12**, 122102 (2005).
- [11] O. Reynolds, *Philos. Trans. R. Soc. London* **170**, 727 (1879).
- [12] J.C. Maxwell, *Philos. Trans. R. Soc. London* **170**, 231 (1879).
- [13] D.W. Hess and K.F. Jensen, *Microelectronics-Processing Chemical Engineering Aspects* (American Chemical Society, Washington D.C., 1989), p. 203.
- [14] S. Musso *et al.*, *J. Cryst. Growth* **310**, 477 (2008).
- [15] Y. Sone, *Phys. Fluids A* **3**, 997 (1991).
- [16] Y. Sone, K. Sawada, and H. Hirano, *Eur. J. Mech., B/Fluids* **13**, no. 3, 299 (1994).
- [17] S. Mitic *et al.*, *Phys. Rev. Lett.* **101**, 235001 (2008).
- [18] T. Ohwada, Y. Sone, and K. Aoki, *Phys. Fluids A* **1**, 1588 (1989).

- [19] T. Ohwada, Y. Sone, and K. Aoki, *Phys. Fluids A* **1**, 2042 (1989).
- [20] S.K. Loyalka, *Phys. Fluids A* **1**, 403 (1989).
- [21] D.H. Papadopoulos and D.E. Rosner, *Phys. Fluids* **7**, 2535 (1995).
- [22] K. Sugiyama *et al.*, *JSME Int. J. Ser. B* **39**, 376 (1996).
- [23] Y. Sone, *Annu. Rev. Fluid Mech.* **32**, 779 (2000).
- [24] C.E. Siewert, *Phys. Fluids* **15**, 1696 (2003).
- [25] S. Takata, S. Yasuda, S. Kosuge and K. Aoki, *Phys. Fluids* **15**, 3745 (2003).
- [26] G.M. Jellum, J.E. Daugherty and D.B. Graves, *J. Appl. Phys.* **69**, 6923 (1991).
- [27] O. Havnes *et al.*, *Plasma Sources Sci. Technol.* **3**, 448 (1994).
- [28] C. Cercignani, *Theory and Application of the Boltzmann Equation* (Scottish Academic Press Ltd., 1975), Chap. 5, p. 255.
- [29] L. Talbot *et al.*, *J. Fluid Mech.* **101**, 737 (1980).
- [30] L.D. Landau and E.M. Lifshitz, *Fluid Mechanics* (Pergamon Press, New York, 1987), Chap. 5, p. 225.
- [31] M. Mikikian *et al.*, *New J. Phys.* **5**, 19 (2003).
- [32] O. Arp *et al.*, *Phys. Rev. Lett.* **93**, 165004 (2004).
- [33] V. Nosenko *et al.*, *Phys. Rev. Lett.* **88**, 135001 (2002).
- [34] J.K. Bhattacharjee, *Convection and Chaos in Fluids* (World Scientific Publishing, Singapore, 1987), Chap. 1, p. 8.
- [35] S. Nunomura, J. Goree, S. Hu, X. Wang, and A. Bhattacharjee, *Phys. Rev. E* **65**, 066402 (2002).
- [36] V. Nosenko, K. Avinash, J. Goree, and B. Liu, *Phys. Rev. Lett.* **92**, 085001 (2004).
- [37] S. Nunomura, J. Goree, and D. Samsonov, *Phys. Rev. Lett.* **84**, pp. 5141-5144 (2000).

- [38] V. Nosenko, J. Goree, Z.W. Ma, and A. Piel, *Phys. Rev. Lett.* **88**, 135001 (2002).
- [39] A. Melzer, M. Klindworth, and A. Piel, *Phys. Rev. Lett.* **87**, 115002 (2001).
- [40] S. Nunomura, J. Goree, S. Hu, X. Wang, A. Bhattacharjee, and K. Avinash, *Phys. Rev. Lett.* **89**, 035001 (2002).
- [41] A. Barkan, R.L. Merlino, and N. D'Angelo, *Phys. Plasmas* **2**, pp. 3563-3565 (1995).
- [42] C. Thompson, A. Barkan, N. D'Angelo, and R.L. Merlino, *Phys. Plasmas* **4**, pp. 2331-2335 (1997).
- [43] N.N. Rao, P.K. Shukla, and M.Y. Yu, *Planet. Space Sci.* **38**, p. 543 (1990).
- [44] V.E. Fortov, A.G. Khrapak, S.A. Khrapak, V.I. Molotkov, A.P. Nefedov, O.F. Petrov, and V.M. Torchinsky, *Phys. Plasmas* **7**, 1374 (2000).
- [45] E. Thomas, R. Fisher, and R.L. Merlino, *Phys. Plasmas* **14**, 123701 (2007).
- [46] P. Bandyopadhyay, G. Prasad, A. Sen, and P.K. Kaw, *Phys. Lett. A* **368**, pp. 491-494 (2007).
- [47] P. Bandyopadhyay, G. Prasad, A. Sen, and P.K. Kaw, *Phys. Rev. Lett.* **101**, 065006 (2008).
- [48] J. Heinrich, S.-H. Kim, and R.L. Merlino, *Phys. Rev. Lett.* **103**, 115002 (2009).
- [49] V.E. Fortov, A.D. Usachev, A.V. Zobnin, V.I. Molotkov, and O.F. Petrov, *Phys. Plasmas* **10**, 1199 (2003).
- [50] M. Schwabe, M. Rubin-Zuzic, S. Zhdanov, H.M. Thomas, and G.E. Morfill, *Phys. Rev. Lett.* **99**, 095002 (2007).
- [51] Chen-Ting Liao, Lee-Wen Teng, Chen-Yu Tsai, Chong-Wai Io, and Lin I, *Phys. Rev. Lett.* **100**, 185004 (2008).
- [52] Lee-Wen Teng, Mei-Chu Chang, Yu-Ping Tseng, and Lin I, *Phys. Rev. Lett.* **103**, 245005 (2009).
- [53] S. Khrapak, D. Samsonov, G. Morfill, H. Thomas, V. Yaroshenko, H. Rothermel, T. Hagl, V. Fortov, A. Nefedov, V. Molotkov, O. Petrov, A. Lipaev, A. Ivanov, and Y. Baturin, *Phys. Plasmas* **10**, 1 (2003).

- [54] A. Piel, M. Klindworth, and O. Arp, Phys. Rev. Lett. **97**, 205009 (2006).
- [55] O. Arp, D. Caliebe, K.O. Menzel, A. Piel, and J. Goree, IEEE Trans. Plasma Sci. **38**, No. 4, p. 842 (2010).
- [56] M. Rosenberg, J. Vac. Sci. Technol. A **14**, 631 (1996).
- [57] P. Epstein, Phys. Rev. **23**, 710 (1924).
- [58] R.L. Merlino, Phys. Plasmas **16**, 124501 (2009).
- [59] T. Trottenberg, D. Block, and A. Piel, Phys. Plasmas **13**, 042105 (2006).
- [60] E. Thomas, Phys. Plasmas **13**, 042107 (2006).
- [61] J.B. Pieper, J. Goree, and R.A. Quinn, Phys. Rev. E **54**, 5636, (1996).
- [62] K.O. Menzel, O. Arp, and A. Piel, Phys. Rev. Lett. **104**, 235002 (2010).
- [63] J.H. Scofield, Am. J. Phys. **62**, 2, 129 (1994).
- [64] A. Piel and A. Melzer, Plasma Phys. Control. Fusion **44**, R1-R26 (2002).
- [65] M. Rosenberg and G. Kalman, Phys. Rev. E **56**, 7166 (1997).
- [66] P.K. Kaw and A. Sen, Phys. Plasmas **5**, 3552.
- [67] M.S. Murillo, Phys. Plasmas **7**, 33 (2000).
- [68] F. Melandsø, Phys. Plasmas **3**, 3890 (1996).
- [69] Xiaogang Wang, A. Bhattacharjee, and S. Hu, Phys. Rev. Lett. **86**, 2569 (2001).
- [70] B. Liu, J. Goree, V. Nosenko, and L. Boufendi, Phys. Plasmas **10**, 9 (2003).
- [71] L.S. Frost, Phys. Rev. **105**, 354 (1957).
- [72] SIGLO-2D version 1.0.
- [73] V.I. Molotkov, A.P. Nefedov, V.M. Torchinski, V.E. Fortov, and A.G. Khrapak, J. Exp. Theor. Phys. **89**, 477 (1999).

- [74] S. Ratynskaia, M. Kretschmer, S. Khrapak, R.A. Quinn, M.H. Thoma, G.E. Morfill, A. Zobnin, A. Usachev, O. Petrov, and V. Fortov, *IEEE Trans. Plasma Sci.* **32**, 613 (2004).
- [75] I. Pilch, T. Reichstein, and A. Piel, *Phys. Plasmas* **16**, 123709 (2009).
- [76] J.D. Williams and E.K. Snipes, *IEEE Trans. Plasma Sci.* **38**, 847 (2010).
- [77] A. Piel, O. Arp, M. Klindworth, and A. Melzer, *Phys. Rev. E* **77**, 026407 (2008).
- [78] V.E. Fortov, O.F. Petrov, V.I. Molotkov, M.Y. Poustylnik, V.M. Torchinsky, V.N. Naumkin, and A.G. Khrapak, *Phys. Rev. E* **71**, 036413 (2005).
- [79] M. Schwabe, S.K. Zhdanov, H.M. Thomas, A.V. Ivlev, M. Rubin-Zuzic, G.E. Morfill, V.I. Molotkov, A.M. Lipaev, V.E. Fortov, and T. Reiter, *New J. Phys.* **10**, 033037 (2008).
- [80] J. Pramanik, B.M. Veerasha, G. Prasad, A. Sen, P.K. Kaw, *Phys. Lett. A* **312**, 84 (2003).
- [81] N.N. Rao and P.K. Shukla, *Planet. Space Sci.* **42**, 221 (1994).
- [82] K.N. Ostrikov, S.V. Vladimirov, M.Y. Yu, and G.E. Morfill, *Phys. Rev. E* **61**, 4315 (2000).
- [83] M.R. Gupta, Susmita Sarkar, Samiran Ghosh, M. Debnath, and Manoranjan Khan, *Phys. Rev. E* **63**, 046406 (2001).
- [84] J.H. Malmberg and C.B. Wharton, *Phys. Fluids* **12**, 2600 (1969).
- [85] K. Mizuno and S. Tanaka, *Phys. Rev. Lett.* **29**, 45 (1972).
- [86] H. Mori, *J. Phys. Soc. Japan* **35**, 592 (1973).
- [87] J.R. Apel, *Phys. Rev. Lett.* **13**, 744 (1967).